scientific reports

Check for updates

OPEN

Lone pair localization governs ferroelectric stability and excitonic properties in lead free halide perovskites

Shahrbano Rahimi & S. Jalali-Asadabadi

Lead free halide perovskites are promising materials for sustainable optoelectronic technologies, but achieving simultaneous control of optical absorption and ferroelectric stability remains challenging. Using $CsGeX_3$ (X = Cl, Br, I) as a model system, we establish a unified microscopic framework that links exciton binding, dielectric screening, and spontaneous polarization to the stereochemically active Ge $4s^2$ lone pair. First principles many body calculations combined with polarization analysis and real space charge mapping reveal that electronic asymmetry rather than lattice tetragonality primarily governs ferroelectric strength across the halide series. Partial Rb substitution acts as a form of chemical pressure that enhances polarization and stabilizes the ferroelectric state while preserving visible light absorption and avoiding mid gap states. In contrast, hydrostatic compression provides a reversible route to tune exciton binding and band gap energies. We show that lone pair localization serves as a transferable descriptor connecting charge redistribution, dielectric response, and excitonic confinement. These findings establish lone pair engineering as a general strategy for designing multifunctional lead free perovskites with coupled optical and ferroelectric functionalities.

All-inorganic halide perovskites have emerged as leading candidates for next-generation optoelectronic and energy-harvesting devices owing to their exceptional photon-to-electricity conversion efficiencies, intrinsic chemical versatility, and environmental resilience[1,2]. In the architecture of perovskite solar cells, the absorber layer—sandwiched between electron- and hole-transporting layers—plays the decisive role in photon capture and exciton generation[3]. The efficiency of this layer is governed jointly by its band-gap alignment, dielectric screening, and carrier dynamics, which together dictate the balance between light absorption, charge separation, and transport[4,5]. Achieving high-performance absorbers therefore requires simultaneous optimization of optical and ferroic properties, demanding a deeper understanding of how electronic correlations, excitonic effects, and lattice distortions intertwine at the atomistic scale[6,7].

Within this family, $CsPbX_3$ (X = Cl, Br, I) has drawn extensive attention for its outstanding optoelectronic performance[8,9] and compatibility with scalable device architectures[10,11]. However, the intrinsic toxicity of Pb[12] and its susceptibility to phase degradation under ambient conditions[13] hinder large-scale deployment. These concerns have fueled the search for lead-free alternatives. Among them, Ge-based halide perovskites $CsGeX_3$ (X = Cl, Br, I) are particularly promising[14–16], combining environmental benignity with polar crystal structures that host ferroelectricity[8,17]. Unlike Pb- and Sn-based counterparts with tolerance factors $t < 1$, which often exhibit octahedral tilts and non-perovskite distortions[13], $CsGeI_3$ with $t > 1$ stabilizes a robust perovskite phase while supporting visible-light absorption and spontaneous polar distortions[13]. Such polar properties further open routes toward ferroelectric photovoltaics, switchable photodetectors, and memory devices[6,7,18–23].

Despite these advantages, a key limitation persists: most prior studies have addressed either band-gap engineering or ferroelectric polarization enhancement in isolation[24–26], overlooking the profound coupling between excitonic physics, dielectric screening, and stereochemical distortions in $CsGeX_3$. In particular, the microscopic role of Ge(II) $4s^2$ lone pairs—a hallmark of second-order Jahn–Teller distortions—remains underexplored as a unifying mechanism linking optical absorption and ferroelectric stability. This gap is critical, as excitonic binding, dielectric anisotropy, and spontaneous polarization all originate from the same underlying redistribution of charge density and orbital hybridization.

Department of Physics, Faculty of Physics, University of Isfahan (UI), Hezar Jerib Avenue, Isfahan 8174673441, Iran. email: sjalali@sci.ui.ac.ir; saeid.jalali.asadabadi@gmail.com

Here we bridge this divide by establishing a unified framework that connects excitonic renormalization, dielectric screening, and ferroelectric energetics through the real-space localization of Ge lone pairs. Specifically, we propose and validate a dual tuning strategy in which partial Rb^+ substitution for Cs^+ (chemical pressure) and hydrostatic compression act as complementary levers to co-engineer optical and ferroic responses. Rb incorporation, owing to its smaller ionic radius, introduces targeted local distortions and modifies electronic topology, while hydrostatic pressure provides a global thermodynamic handle for optimizing exciton dynamics and ferroelectric stability[27–29]. This concept is supported by earlier demonstrations of A-site substitution effects in Rb-based perovskites[30,31], Mn^{2+} doping[32], and Sb/Eu alloying[33,34], but here we systematically integrate such approaches with excitonic and ferroelectric control.

To realize this program, we employ a multiscale *ab initio* framework combining density functional theory (DFT)[35,36] with many-body perturbation theory (MBPT)[37] in the GW plus Bethe–Salpeter equation (GW+BSE) formalism for predictive optical spectroscopy. Berry-phase analysis provides quantitative polarization, while Bader charge decomposition and electron localization function (ELF) mapping uncover bonding and lone-pair activity. We use a custom Python-based image-processing pipeline to normalize ELF metrics, enabling quantitative comparison of lone-pair localization across halides. This combination uniquely disentangles the intertwined roles of geometry, correlation, and substitution in controlling excitonic and ferroic properties.

Our results reveal that chemical pressure deepens the ferroelectric double-well, enhances spontaneous polarization, and simultaneously sharpens excitonic resonances by suppressing dielectric screening. Hydrostatic pressure, conversely, delocalizes excitons, reduces E_b^{ex}, and softens ferroelectric barriers. By linking Bader charges, ELF-derived lone-pair indices, and many-body optical spectra, we show that electronic asymmetry—not lattice distortion magnitude—is the decisive driver of ferroelectric and excitonic performance. These insights elevate lone-pair localization to a quantitative design parameter and establish Rb-doped $CsGeX_3$ as a versatile lead-free platform for co-optimized optoelectronic and ferroic functionalities.

Exciton–plasmon coevolution under chemical pressure and hydrostatic strain

Figures 1 shows how excitonic absorption and plasmonic dielectric loss coevolve when the dielectric environment of $CsGeX_3$ perovskites is tuned by A-site chemical pressure (Cs→Rb) and hydrostatic strain. Panels (a_i–c_i) resolve the tensorial dielectric function within GW+BSE, while panels (d_i) display the energy-loss function $\Im[-1/\varepsilon(\omega)]$. Together, they demonstrate that excitonic and plasmonic responses are not separate phenomena but two linked outcomes of the same frequency-dependent screening landscape.

In the GW+BSE framework—summarized in "Many-Body Perturbation Theory for Optical Excitations" and detailed in "SM8" and illustrated in Figs. 6, SM1, and SM5—the quasiparticle energies corrected via Eq. (8) constitute the diagonal block of the excitonic Hamiltonian [Eq. (11)], while the screened-direct term $H^{(c)}$ in Eq. (13) provides the attractive interaction responsible for exciton binding. Here, "SM" denotes the Supplemental Material. The macroscopic dielectric response is constructed from excitonic amplitudes via Eq. (19), and the exciton binding energy E_b^{ex} is defined by Eq. (23). The trends follow the hydrogenic scaling $E_b^{\mathrm{ex}} \propto \mu/\varepsilon^2(0)$ [Eq. (25)].

Within the GW+BSE framework, the screened electron-hole interaction is constructed using the electronic dielectric function ε_∞, while lattice polarization from soft ferroelectric phonons is not explicitly included; the implications of this approximation for exciton stability are discussed in "Role of Dielectric Screening and Lattice Polarization in Exciton Binding".

Panels (a_i–c_i) show that including $H^{(c)}$ produces bright sub-gap excitons, especially in $CsGeCl_3$ and $CsGeBr_3$, lying up to 0.26 eV below E_g^{GW}. The oscillator strengths $|t_{\lambda\mu}|^2$ in Eq. (20) are strongly polarized, redistributing spectral weight to the lowest singlets. This renormalizes $\Re[\varepsilon(\omega \to 0)]$ relative to RPA, proving that excitons modify static screening itself. Along the halogen series Cl→Br→I, larger $\varepsilon(0)$ and lighter reduced masses μ lower E_b^{ex}, progressively shifting excitons toward the continuum, exactly as predicted by Eq. (25). The anisotropy in panels (c_i), with ε_{zz} dominating Br and I but not Cl, directly tracks the alignment of excitons with the rhombohedral polar axis, making the optical tensor a proxy for ferroelectric order.

Chemical pressure by Rb substitution acts selectively. In $CsGeCl_3$, Rb sharpens the lowest BSE peak and redshifts the main ELOSS maximum [panel (d_1)], signaling stronger exciton confinement and reduced dielectric loss. No spurious mid-gap weight appears in the RPA–BSE comparison, confirming alloying perturbs screening without compromising band-edge purity, consistent with the DOS analysis in "Orbital control of excitons, screening, and ferroelectricity: insights from the projected DOS". In Br- and I-based compounds, however, the intrinsically larger static dielectric constant $\varepsilon(0)$ screens the perturbation induced by Rb substitution, leaving the ELOSS spectra nearly unchanged, where, "static" refers to the zero-frequency response of the material to a slowly varying external field, for which ionic positions can relax adiabatically. This shows that chemical pressure is an effective tuning lever only in rigid, weakly screening lattices, whereas its influence becomes negligible in soft, highly polarizable halide frameworks. For completeness, formation energies associated with these substitutions are listed in Table SM1.

Hydrostatic compression exerts the opposite influence across all halides: excitonic resonances weaken, ELOSS peaks blueshift and broaden, and exciton binding energies E_b^{ex} decrease. Microscopically, compression steepens quasiparticle dispersions in Eq. (11) and enhances screening in W [Eq. (14)], thereby weakening the screened-direct interaction $H^{(c)}$ and reducing exciton confinement. Consistent pressure-driven blueshifts of loss and plasmonic features, accompanied by increases in $\varepsilon(0)$, have also been reported for Sb_2S_3 under hydrostatic compression[38]. This trend reflects enhanced orbital overlap and increased band-edge dispersion, promoting greater polarizability and electronic delocalization—consistent with similar observations in Refs.[39–41].

The chloride system provides the clearest demonstration: at ambient conditions, its lowest exciton is $\sim$ 0.26 eV bound and thermally stable at room temperature. Upon hydrostatic compression, the excitonic redshift diminishes and the ELOSS peak moves to higher energy, indicating reduced confinement and enhanced

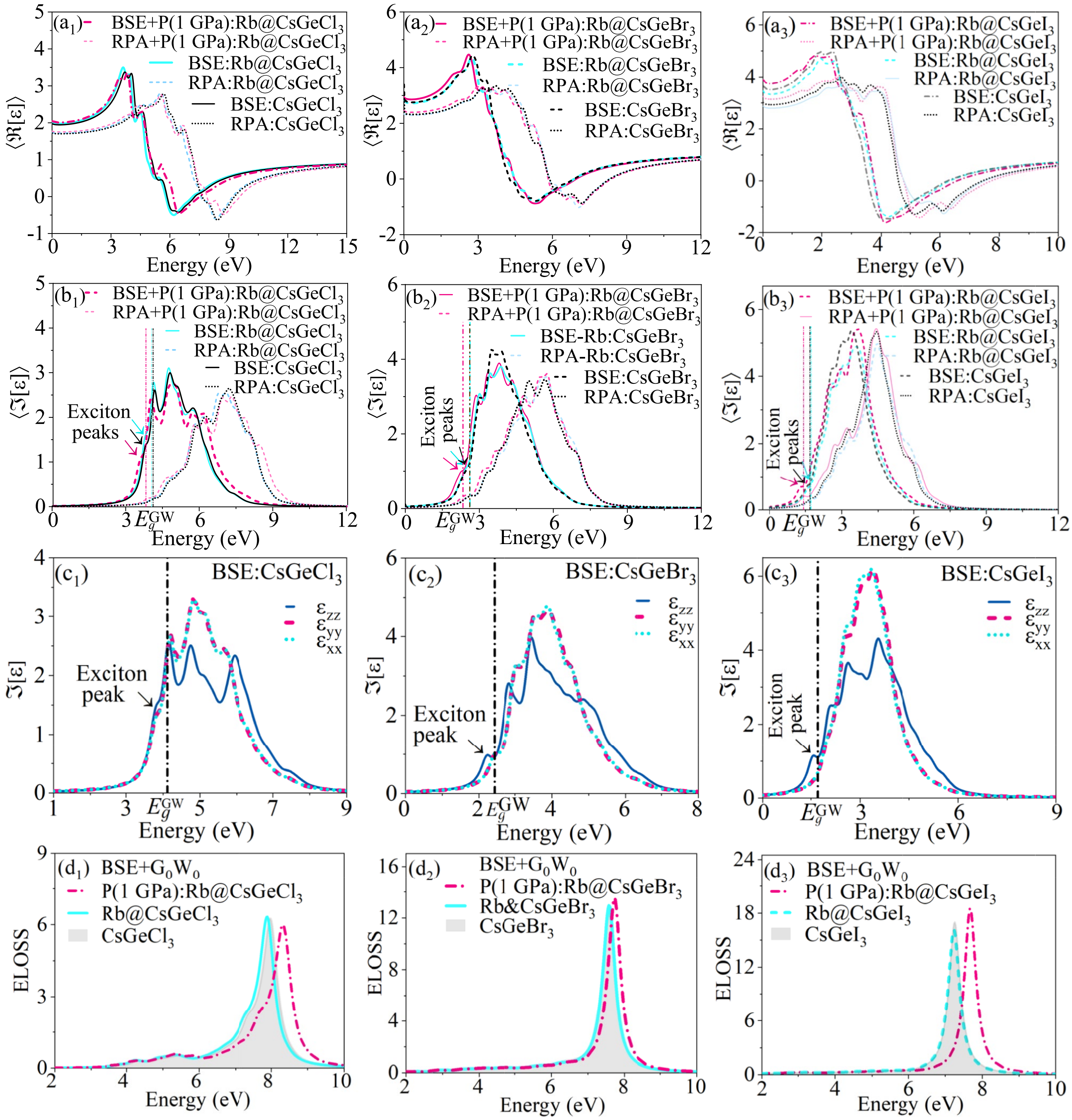

Fig. 1. Excitonic and plasmonic responses of $CsGeX_3$ halide perovskites under chemical substitution and pressure. ($\mathbf{a}_i, \mathbf{b}_i, \mathbf{c}_i, i = 1, 2, 3$) GGA+GW+BSE dielectric spectra reveal pronounced sub-gap excitonic resonances, anisotropy, and systematic tuning of screening with 16.7% Rb substitution at the Cs site and hydrostatic compression. ($\mathbf{d}_i, i = 1, 2, 3$) ELOSS spectra show a redshift in Rb-doped $CsGeCl_3$ and pressure-driven blueshifts across all halides, accompanied by enhanced dielectric damping and modified plasmonic activity, establishing chemical and mechanical routes to control many-body optical excitations.

screening. In contrast, Rb substitution restores exciton localization and suppresses dielectric loss, revealing that strain and alloying act as complementary, reversible levers for tuning between exciton- and carrier-dominated regimes. Notably, Rb substitution induces a distinct redshift in $CsGeCl_3$, while the Br- and I-based analogues remain largely unchanged, implying minimal impact on leakage. The chloride's downward ELOSS shift is consistent with Ref.[42], where lower-energy plasmon peaks correlate with suppressed charge leakage and improved polarization retention. This correspondence underscores that chemical pressure in $CsGeCl_3$ not only enhances exciton confinement but also strengthens dielectric and ferroelectric integrity.

Figures 1, SM7 , and SM9 together provide a coherent picture: both exciton binding and plasmonic energy loss can be systematically tuned through the static dielectric constant $\varepsilon(0)$, the reduced mass μ, and the underlying lattice polarizability. Chemical pressure deepens excitons and lowers loss in rigid lattices, while hydrostatic strain delocalizes excitons and raises plasmon energies in softer hosts. Because both knobs act without introducing mid-gap states, they enable the co-optimization of radiative coupling, dielectric loss, and ferroelectric stability within the same lead-free perovskite framework.

These results collectively establish $CsGeI_3$ as a lead-free analog to $CsPbI_3$ in solar cell applications, sharing similar E_b^{ex} values (0.1–0.2 eV) and comparable dielectric behavior[43,44]. The tight agreement of our G_0W_0+BSE energetics with G_3W_0+BSE[3] and experiment[1,28,45] illustrates the differential robustness of $E_b^{\mathrm{ex}} = E_g^{\mathrm{e}} - E_g^{\mathrm{opt}}$ against method-dependent absolute errors, making it a reliable design variable across codes and protocols. In contrast, $CsGeCl_3$—with its higher $E_b^{\mathrm{ex}} = 0.260$ eV, low $\varepsilon(0) = 1.98$, and sharp BSE exciton resonances just below the QP gap—represents the strongly bound, exciton-bright limit.

Bridging excitonic and quasiparticle regimes in lead-free $CsGeX_3$ perovskites through chemical and strain engineering

Figures 2(a)-(e) unify multiple complementary views of the band-edge physics governing light–matter interaction in $CsGeX_3$ (X = Cl, Br, I): (a) method-aware benchmarks of quasiparticle and optical gaps, (b) BSE optical gaps E_g^{opt}, (c) ambient-pressure exciton binding energies E_b^{ex}, and the strain response of (d) E_g^{GW} and (e) E_b^{ex}. Read together with the dielectric and ELOSS spectra in Fig. 1, this figure demonstrates that E_b^{ex} serves as a predictive and transferable descriptor that connects dielectric screening, effective-mass renormalization, and lattice polarizability to device-relevant performance metrics. See also Figs. SM8 and SM3, as well as Table SM2.

At zero pressure, the chemical hierarchy is robust across levels of theory: moving from Cl to I, E_g^{e} narrows (from ~ 4.1 to ~ 1.7 eV in G_0W_0), and E_b^{ex} weakens (from ~ 0.26 to ~ 0.12 eV). This co-variation is quantitatively captured by the hydrogenic scaling $E_b^{\mathrm{ex}} \propto \mu/\varepsilon^2(0)$, with the heavier halide enhancing the static dielectric constant ($\varepsilon(0) \approx 1.98 \rightarrow 3.53$) and promoting Ge–X delocalization that lowers the reduced mass μ. The excitonic redshift $\Delta_{\mathrm{ex}} = E_g^{\mathrm{opt\text{-}RPA}} - E_g^{\mathrm{opt\text{-}BSE}}$ coincides with E_b^{ex} and thus provides a direct spectral handle on electron–hole attraction. These energy scales are technologically decisive: in $CsGeCl_3$ and $CsGeBr_3$, $E_b^{\mathrm{ex}} \gg k_BT$ at 300 K ensures thermally stable excitons with large oscillator strength, underpinning efficient emission and polariton formation; in $CsGeI_3$, $E_b^{\mathrm{ex}} \sim 0.1$ eV supports partial thermal ionization and hence more efficient charge extraction for photovoltaics. Spin–orbit coupling provides a secondary, halide-dependent tuning: it narrows E_g^{e} in all cases, but its impact on E_b^{ex} depends on the relative SOC-induced renormalization of the QP and optical gaps. In $CsGeCl_3$, SOC reinforces exciton stability by maintaining a large gap offset, whereas in $CsGeBr_3$ and $CsGeI_3$ it softens binding by reducing the separation between the quasiparticle and optical thresholds.

Partial Rb substitution at the A site preserves this hierarchy while introducing only small, rigid shifts in both E_g^{e} and E_b^{ex} (tens of meV) without generating mid-gap states. This "clean" alloying behavior confirms that Rb primarily reweights screening and local strain rather than altering the band-edge topology. In practice, this is advantageous: the chloride retains large E_b^{ex} for emissive platforms with slightly improved confinement, whereas the iodide preserves low E_b^{ex} for solar conversion, enabling compositional trims without compromising the intended operating regime.

Hydrostatic compression acts as a continuous dial for co-tuning E_g^{GW} and E_b^{ex} along phase-stable trajectories, as shown in panels (d) and (e). For Rb@$CsGeCl_3$, an $\sim 8\%$ volume reduction drives E_g^{GW} from ~ 4.06 to ~ 3.61 eV and E_b^{ex} from 0.268 to 0.081 eV. These changes are near-linear over the explored range, yielding practical coefficients $\partial E_g/\partial(\Delta V/V) \approx -0.055$ eV/% and $\partial E_b/\partial(\Delta V/V) \approx -0.023$ eV/%. The microscopic origin is twofold: compression enhances Ge–X overlap and band-edge dispersion (entering the diagonal BSE block), while simultaneously increasing $\varepsilon(0)$ and weakening the attractive $H^{(\mathrm{c})}$ kernel; the screening term dominates the hydrogenic balance and drives the net decrease of E_b^{ex}. Br- and I-based systems show smaller absolute slopes, as expected for softer, more polarizable lattices that start with larger $\varepsilon(0)$. The rapid approach of the chloride's E_b^{ex} to Br/I values under modest strain demonstrates a controllable cross-over from an exciton-bright to a carrier-bright regime within a single composition, enabling reversible toggling between LED/polaritonic and photovoltaic (PV)-like operation.

The energetic trends in Fig. 2 close the loop with the macroscopic spectra in Fig. 1. Larger E_b^{ex} (chloride, low pressure) correlates with sharp, polarized BSE peaks dominated by ε_{zz} and with suppressed ELOSS; smaller E_b^{ex} (iodide, higher screening or under compression) maps onto broadened excitons and enhanced dielectric loss. The selective ELOSS redshift observed upon Rb substitution in the chloride is consistent with its stronger excitonic confinement and more tunable screening, whereas the Br and I analogues remain comparatively inert to A-site alloying. This one-to-one correspondence indicates that excitons and plasmons are co-governed by the same frequency-dependent screening landscape, allowing joint optimization of radiative coupling and loss.

For readers focused on practice and metrology, the figure provides several actionable quantifiers. First, the excitonic redshift Δ_{ex} is a directly measurable proxy for E_b^{ex} from optical spectra. Second, the dimensionless ionization ratio E_b^{ex}/k_BT separates emissive ($\gg 1$) from dissociative (~ 1) operation and can be targeted by strain with the linear coefficients above. Third, the tight agreement of our G_0W_0+BSE energetics with G_3W_0+BSE[3] and experiment[1,28,45] illustrates the differential robustness of $E_b^{\mathrm{ex}} = E_g^{\mathrm{e}} - E_g^{\mathrm{opt}}$ against method-dependent absolute errors, making it a reliable design variable across codes and protocols.

In sum, Fig. 2 elevates E_b^{ex} from a spectroscopic observable to a design coordinate that continuously connects chemical choice (halide identity), clean alloying (Rb), and reversible mechanical control (hydrostatic or epitaxial strain) with device intent. Chloride- and bromide-based compounds provide large, anisotropic, radiatively efficient excitons for emission and polaritonics, while iodide-based materials favor photovoltaic charge separation; strain moves a given composition smoothly along this continuum without triggering phase

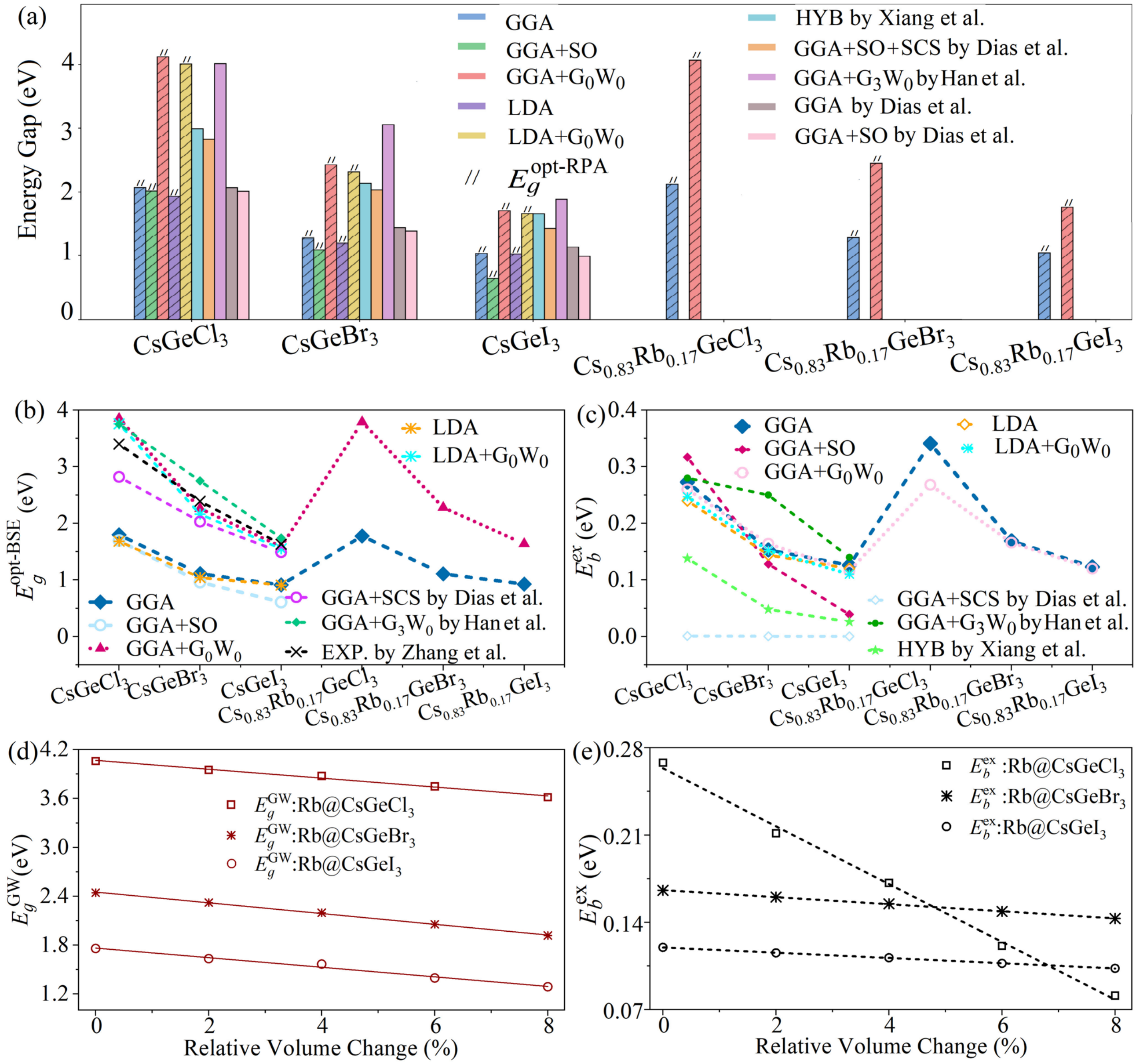

Fig. 2. Electronic and optical gaps with zero- and finite-pressure excitonics in pristine and Rb-doped $CsGeX_3$ perovskites. (**a**) Quasiparticle electronic band gaps E_g^e (solid bars) and optical RPA gaps $E_g^{\text{opt}-\text{RPA}}$ (hatched bars) for pristine and Rb-doped compounds, compared across computational approaches and literature. (**b**) BSE Optical gaps E_g^{opt} and (c) zero-pressure exciton binding energies E_b^{ex}, benchmarked between our EXCITING-based results, VASP calculations, and experiments[1,3,14,46]. Pressure dependence of (d) E_g^{GW} and (e) E_b^{ex}, exhibiting a monotonic decrease under hydrostatic compression (relative volume reduction), consistent with enhanced dielectric screening and increased band-edge dispersion. The Cl-based system shows the strongest excitonic tunability, with E_b^{ex} approaching that of the Br- and I-based analogues under moderate strain.

change or defect states. This integrated, quantitatively calibrated picture enables predictive co-design of excitonic strength, optical onset, polarization anisotropy, and dielectric loss in lead-free halide perovskites.

Orbital control of excitons, screening, and ferroelectricity: insights from the projected DOS

Figures 3 and SM10 provide the microscopic electronic context underlying the excitonic, dielectric, and loss spectra shown in Figs. 1 and 2. Given the consistent DOS features across the $CsGeX_3$ series, Rb-doped $CsGeBr_3$ is chosen as a representative prototype to unravel the electronic origins of the optical response. Orbital- and atom-resolved decompositions reveal how specific chemical channels and Ge–X hybridizations generate the

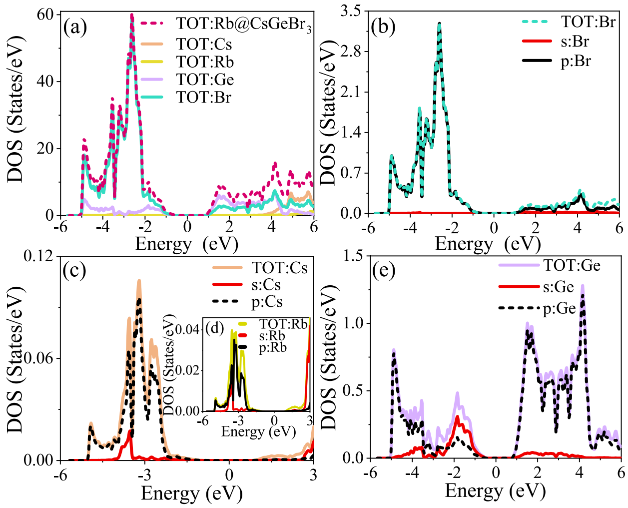

Fig. 3. Projected and total DOSs for Rb-doped $CsGeBr_3$, computed using the SCAN functional. Panel (**a**) shows the total DOS and atomic projections from Cs, Rb, Ge, and Br. Panels (**b**–**e**) decompose the orbital contributions: (**b**) Br-*s* and Br-*p* states, (**c**) Cs-*s* and Cs-*p*, (**d**) Rb-*s* and Rb-*p*, and (**e**) Ge-*s* and Ge-*p*. The Fermi level is set to 0 eV. These plots reveal the dominant orbital characters near the valence and conduction edges, clarify the impact of Rb substitution, and highlight the role of lone-pair activity in structural distortion and polarization.

bright sub-gap resonances and enable systematic tuning of E_b^{ex}. These trends provide a direct microscopic design pathway for controlling excitonic behavior in lead-free halide perovskites, as shown in Figs. 3, SM2, and SM10 .

The valence band maximum is dominated by Br-*p* states that mix with non-negligible Ge-*s* character, while the conduction band minimum originates mainly from Ge-*p* orbitals. Neither Cs nor Rb contributes electronic weight at the band edges, confirming that the A-site acts as a structural and electrostatic scaffold rather than as a direct participant in optical transitions. This *p*–(*s*,*p*) alignment maximizes the dipole matrix elements in Eq. (20), explaining the intense and polarization-selective excitonic resonances observed in Fig. 1(b_i,c_i). The absence of impurity-derived states at the band edges further clarifies why Rb substitution modifies dielectric screening and narrows ELOSS linewidths [Fig. 1(d_i)] without degrading radiative efficiency. These observations confirm that the excitonic redshifts and dielectric anisotropy reported earlier are intrinsic many-body effects rather than artifacts of doping-induced states.

The orbital projections also clarify why halogen substitution controls the magnitude and tunability of the exciton binding energy E_b^{ex}. In $CsGeBr_3$, Br-*p*–Ge-*s* hybridization broadens the valence band and enhances spatial overlap with Ge-*p* conduction states, thereby increasing the screened direct term $H^{(\mathrm{c})}$ in the BSE Hamiltonian [Eq. (13)] and amplifying the oscillator strength of the lowest excitons. Replacement of Br by I increases orbital diffuseness and polarizability, which raises $\varepsilon(0)$ and reduces the reduced mass μ, lowering E_b^{ex} according to the hydrogenic scaling $E_b^{\mathrm{ex}} \propto \mu/\varepsilon^2$ [Eq. (25)]. Substituting Br with Cl has the opposite effect: it suppresses screening, narrows the Ge-*p* conduction manifold, increases effective masses, and strengthens Coulomb binding. This orbital-level picture mirrors the quantitative hierarchy extracted in Fig. 2(c) and explains the exceptional strain sensitivity of the chloride in Fig. 2(e), where compression enhances Ge–X overlap, increases $\varepsilon(0)$, and drives exciton delocalization in near-linear correlation with the blueshifts in ELOSS.

Another key feature revealed in Fig. 3 is the non-negligible Ge-*s* intensity near the valence edge, a direct fingerprint of the stereochemically active Ge(II) lone pair. This asymmetric density distribution promotes off-centering of the Ge atoms within the GeX_6 octahedra and stabilizes the polar *R*3*m* phase (see "Doping-Driven Structural Distortions in Rb-Substituted $CsGeX_3$ Halide Perovskites" and Figs. 8 and SM6). The same asymmetry enhances out-of-plane dipole transitions, consistent with the dominance of ε_{zz} in Fig. 1(c_i) and reinforcing the link between lattice polarization and excitonic anisotropy. Rb substitution, through its smaller ionic radius, contracts the A-site cavity and sharpens Ge–X hybridization, thereby modulating lone-pair activity without introducing new electronic states at the band edges. This mechanism explains why Rb doping simultaneously deepens ferroelectric wells, enhances polarization, and modifies the excitonic response, as captured by Figs. 4 and 5.

These results close the loop between electronic structure and macroscopic response. The orbital characters at the band edges define the interband phase space, while the BSE kernel [Eq. (10)] redistributes oscillator strength to form discrete excitonic peaks that redshift absorption relative to E_g^{GW} [Eq. (8)]. Variations in orbital overlap driven by halogen chemistry, Rb substitution, or hydrostatic pressure directly modulate μ and $\varepsilon(0)$, which in turn control exciton binding, dielectric screening, plasmonic dissipation, and ferroelectric softness.

From a design perspective, this orbital mapping provides explicit chemical guidance. Chloride and bromide compounds with localized *p*–*s* mixing and smaller $\varepsilon(0)$ maximize exciton stability, radiative coupling, and polarization robustness, making them suited for emitters, polaritonic devices, and non-volatile memories. Iodide-rich or compressed structures with broader *p* manifolds and larger $\varepsilon(0)$ favor free-carrier generation, dielectric

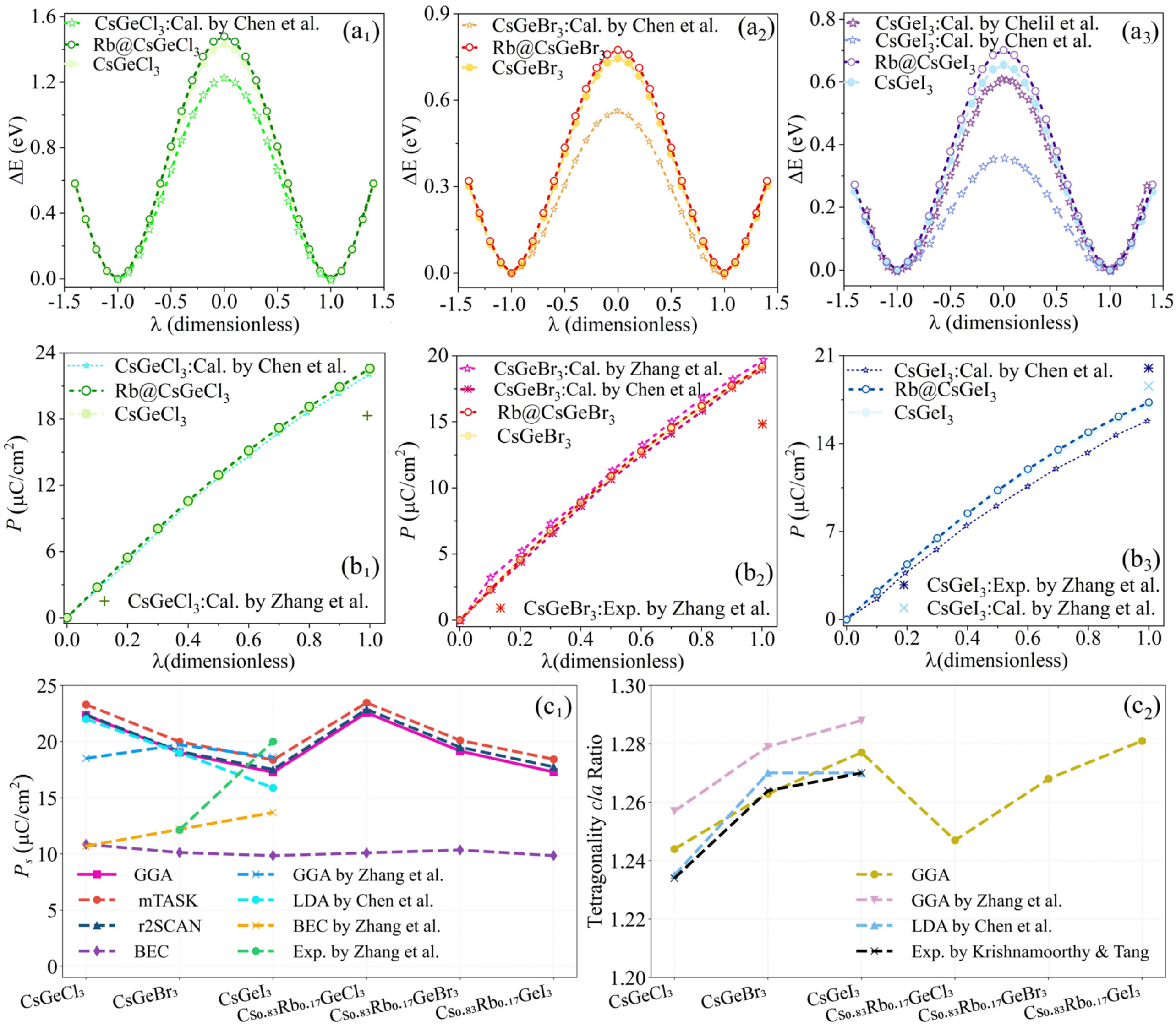

Fig. 4. Chemical pressure enhances ferroelectric stability in $CsGeX_3$ halide perovskites. ($\mathbf{a}_1$)-($\mathbf{a}_3$) Double-well energy profiles $\Delta E(\lambda)$ for $CsGeX_3$ (X = Cl, Br, I) and Rb-substituted analogues show the characteristic displacive ferroelectric topology with unstable paraelectric states at $\lambda = 0$ and degenerate minima at $\lambda = \pm 1$. Rb substitution deepens and stiffens the wells, particularly in $CsGeCl_3$, evidencing enhanced ferroelectric robustness under chemical pressure. The calculated barrier heights agree closely with previous FP-LAPW[50] and plane-wave[17] results. ($\mathbf{b}_1$)-($\mathbf{b}_3$) Berry-phase polarization $P(\lambda)$ increases monotonically along the structural distortion path, confirming strengthened polarization retention and coherent switching behavior upon Rb incorporation. The comparison with prior theory and experiment[1] shows excellent consistency in both magnitude and trend. Correlation between ($\mathbf{c}_1$) spontaneous polarization P_s and ($\mathbf{c}_2$) tetragonality *c*/*a*, evaluated from PBE-GGA, mTASK, r2SCAN, and BEC methods, reveals that while Rb substitution slightly increases *c*/*a*, the dominant enhancement in P_s originates from electronic asymmetry rather than geometric strain. The results of the pristine compounds are in quantitative agreement with experimental and computational reports[1,17,50,51].

loss, and photovoltaic operation. Rb substitution serves as a chemically clean lever for tuning polarization and screening without compromising band-edge purity. In this way, Fig. 3 situates the orbital-resolved electronic structure as the microscopic origin of the coupled excitonic, dielectric, and ferroic behaviors that define the design principles of $CsGeX_3$ perovskites.

Formation energetics and clean alloying behavior of Rb substitution

A central premise of this work is that partial Rb substitution on the A site of $CsGeX_3$ acts as a *clean chemical pressure*, modifying lattice stiffness and electronic screening without introducing defect-induced mid-gap states. Here, we clarify the physical meaning of “clean” alloying and provide an energetic justification for the thermodynamic feasibility of Rb incorporation at experimentally relevant concentrations.

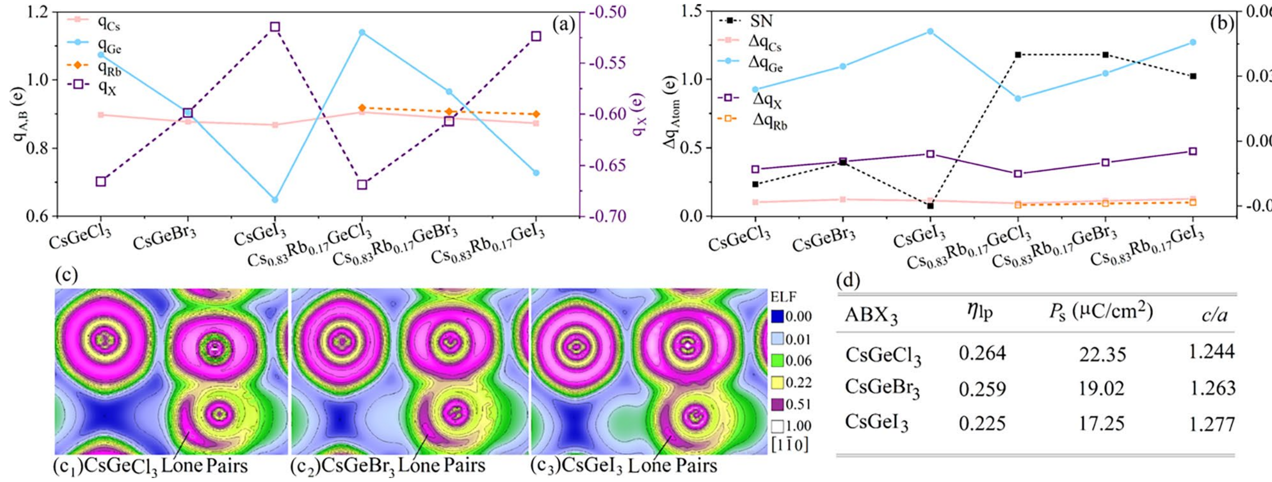

Fig. 5. Charge redistribution and lone-pair driven ferroelectricity in $CsGeX_3$ halide perovskites. (**a**) Bader charges $q_{\mathrm{A,B,X}}$ for pristine and Rb-doped compounds, where A = Cs/Rb, B = Ge, and X = Cl, Br, or I in the ABX_3 perovskite lattice. (**b**) Deviations from formal ionic values, $|\Delta q_{\mathrm{Atom}}| = |q_{\mathrm{Atom}}^{\mathrm{Crystal}} - q_{\mathrm{Atom}}^{\mathrm{Free\ Space}}|$, with stoichiometric neutralization (SN) confirming unit-cell charge balance. ($\mathbf{c}_i$, $i = 1$–3) ELF contour maps for $CsGeCl_3$, $CsGeBr_3$, and $CsGeI_3$ on the $[1\bar{1}0]$ plane, highlighting Ge-centered lone pairs as regions of enhanced localization. (**d**) normalized lone-pair localization index $\eta_{\mathrm{lp}} = A_{\mathrm{lp}}/A_{\mathrm{ELF}}$, where A_{lp} is the ELF-active area assigned to Ge lone pairs and A_{ELF} is the total ELF-active area, correlated with spontaneous polarization P_s and tetragonality (*c*/*a*). These results show that electronic asymmetry from lone-pair localization, rather than lattice distortion, is the primary driver of ferroelectricity across the halide series.

Compound	$\mathbf{Cs_{0.83}Rb_{0.17}GeCl_3}$	$\mathbf{Cs_{0.83}Rb_{0.17}GeBr_3}$	$\mathbf{Cs_{0.83}Rb_{0.17}GeI_3}$
E_{form} (eV/f.u.)	-14.84	-12.45	-9.14

Table 1. Formation energies of substitutional Rb alloying in $CsGeX_3$ perovskites. Formation energies E_{form} (in eV per formula unit) of $Cs_{0.83}Rb_{0.17}GeX_3$ relative to pristine $CsGeX_3$ and elemental Rb. Negative values indicate thermodynamically favorable A-site substitution. The monotonic reduction in $|E_{\mathrm{form}}|$ from Cl to I reflects increasing lattice softness and reduced cohesive energy for heavier halides.

Rb substitution is isovalent with Cs (Rb^+ vs. Cs^+) and occurs on the electronically inactive A site of the perovskite lattice. Consequently, the band edges—which are dominated by Ge–*p* and X–*p* states—are not directly perturbed by A-site alloying. This is confirmed by the projected density of states (Fig. 3), which shows no Rb-derived states within the band gap or near the band edges for $Cs_{0.83}Rb_{0.17}GeX_3$ across the halide series. In this context, "clean" alloying refers specifically to the absence of dopant-induced electronic trap states, rather than to the absence of local structural disorder.

To quantify the thermodynamic feasibility of substitutional Rb alloying, we define an A-site substitution (alloy-formation) energy referenced to the pristine host and elemental reservoirs,

$$E_{\mathrm{form}}(x) = \frac{1}{N_{\mathrm{f.u.}}}\Big[E_{\mathrm{tot}}(\mathrm{Cs}_{1-x}\mathrm{Rb}_x\mathrm{GeX}_3) - E_{\mathrm{tot}}(\mathrm{CsGeX}_3) - N_{\mathrm{Rb}}\mu_{\mathrm{Rb}} + N_{\mathrm{Rb}}\mu_{\mathrm{Cs}}\Big], \tag{1}$$

where E_{tot} denotes the DFT total energy of the corresponding relaxed structure, μ_{Rb} and μ_{Cs} are the chemical potentials of Rb and Cs taken from their stable elemental reference phases (metallic Rb and metallic Cs), and N_{Rb} is the number of substituted Rb atoms in the simulation cell. The factor $N_{\mathrm{f.u.}}$ is the number of $CsGeX_3$ formula units contained in the alloy supercell, so that E_{form} is reported in eV per formula unit (eV/f.u.). In our case, the representative dilute composition $Cs_{0.83}Rb_{0.17}GeX_3$ corresponds to replacing one Cs atom by one Rb atom in a supercell containing $N_{\mathrm{f.u.}} = 6$ formula units, i.e., $x = N_{\mathrm{Rb}}/N_{\mathrm{A}} = 1/6 \simeq 0.167$ with $N_{\mathrm{Rb}} = 1$. Total energies produced by the electronic-structure code in Rydberg units are converted to electronvolts using $1\ \mathrm{Ry} = 13.605693$ eV, and the resulting energy difference is divided by $N_{\mathrm{f.u.}}$ to obtain E_{form} in eV/f.u. (For completeness, one may alternatively report a substitution energy per dopant, $E_{\mathrm{form}}^{(\mathrm{per\ Rb})} = N_{\mathrm{f.u.}}\, E_{\mathrm{form}}/N_{\mathrm{Rb}}$, which is equivalent to Eq. (1) without the $1/N_{\mathrm{f.u.}}$ prefactor.)

To assess the thermodynamic viability of Rb incorporation, we evaluated the formation energetics of substitutional Rb on the Cs site at a representative dilute concentration ($x \approx 0.17$). Table 1 summarizes the calculated formation energies of $Cs_{0.83}Rb_{0.17}GeX_3$ relative to the corresponding pristine $CsGeX_3$ host and elemental Rb. All three compounds exhibit negative formation energies, indicating that Rb substitution on the A site is energetically favorable and does not require compensating charged defects to stabilize the lattice.

The decreasing magnitude of E_{form} from Cl to I follows the expected chemical trend of weakening Ge–X bonds and enhanced anion polarizability, which also underpins the evolution of dielectric screening and excitonic behavior discussed in "Exciton–plasmon coevolution under chemical pressure and hydrostatic strain". Importantly, the consistently negative formation energies demonstrate that Rb incorporation is thermodynamically allowed across the halide series and does not drive the system toward defect-compensated or electronically disruptive configurations.

Low-level Rb incorporation has also been extensively explored experimentally in mixed Pb–halide perovskites, where Rb—despite being too small to form a stable perovskite lattice on its own—preferentially stabilizes mixed-cation compositions when combined with Cs and organic A-site cations. Such systems exhibit enhanced power-conversion efficiency and improved structural and thermal stability, without evidence of mid-gap states or detrimental electronic trap formation[47–49]. These observations support the general interpretation of Rb as a benign, isovalent A-site dopant that primarily influences lattice geometry and stability rather than band-edge electronic structure. In the present work, our first-principles results indicate that a similar role is played by Rb in Ge-based halide perovskites, where substitutional Rb acts as a clean chemical-pressure agent while preserving favorable electronic properties.

While a full defect phase-diagram analysis is beyond the scope of this work, the combination of (i) isovalent A-site substitution, (ii) negative alloy formation energetics, and (iii) the absence of dopant-induced gap states in the electronic structure provides strong evidence that Rb substitution constitutes a *clean* and experimentally feasible tuning mechanism. In practice, Rb acts primarily as an internal chemical pressure that modifies lattice geometry and polar distortions without introducing mid-gap trap states that would degrade ferroelectric or excitonic functionality.

Chemical pressure as a dual lever for ferroelectric stability and excitonic coupling in $CsGeX_3$ perovskites

Figure 4 integrates, in one coherent framework, the three central descriptors of ferroelectric stability in $CsGeX_3$ halide perovskites: the double-well energy topology $\Delta E(\lambda)$, the Berry-phase polarization pathway $P(\lambda)$, and the spontaneous polarization P_s correlated with tetragonality *c*/*a*. Here, tetragonality refers to deviations in the *c*/*a* ratio within the hexagonal representation of the *R*3*m* phase, serving as a structural proxy for lattice anisotropy. Together, these panels expose the microscopic physics of lattice instabilities, the electronic origin of polarization, and the macroscopic indicators of structural anisotropy, while clarifying how Rb substitution acts as a form of chemical pressure that reshapes the entire ferroelectric landscape. For further details, see Secs. SM5, SM6, and SM11B; Figs. SM11, SM12, and SM13; and Listings 1, 2, and 3.

Panels (a_1)-(a_3) reveal the expected symmetric double-well potential characteristic of displacive ferroelectrics, featuring an unstable paraelectric configuration at $\lambda = 0$ and degenerate ferroelectric minima at $\lambda = \pm 1$; see also Fig. SM4. The barrier height $\Delta E_{\mathrm{barrier}}$ decreases systematically from Cl to I, with 47.66, 24.83, and 21.66 meV/atom for $CsGeCl_3$, $CsGeBr_3$, and $CsGeI_3$, respectively. Rb substitution deepens the wells and sharpens their curvature, especially in $CsGeCl_3$, indicating enhanced ferroelectric stability under chemical pressure. This behavior follows the Landau–Devonshire expansion $F(P) = \alpha P^2 + \beta P^4 + \ldots \quad (\alpha < 0,\ \beta > 0)$[52], where a deeper well implies larger $|\alpha|/\beta$, and curvature $|\partial^2 \Delta E/\partial \lambda^2|_{\lambda \to \pm 1}$ scales inversely with dielectric susceptibility. The increase in $\Delta E_{\mathrm{barrier}}$ strengthens retention against thermal back-switching, with coercive field $E_c \propto \Delta E_{\mathrm{barrier}}/(P_s\, \xi)$, ξ being the domain-wall width. Physically, the smaller Rb^+ ion induces lattice contraction, reinforcing Ge–X bonding and enhancing the stereochemical activity of the Ge *s* lone pair—the origin of the second-order Jahn–Teller distortion. Our PBE-GGA barriers agree quantitatively with prior works: for $CsGeI_3$, the computed 21.66 meV/atom matches 20.3 meV/atom from Chelil *et al.*[50] (FP-LAPW, WIEN2ĸ) and 18.4 meV/atom from Chen *et al.*[17] (VASP. Likewise, our $CsGeBr_3$ polar–nonpolar difference agrees with $\sim$ 85 meV/f.u. ($\approx$17 meV/atom) from Zhang *et al.*[1]. These consistencies confirm the robustness of our structural energetics. Overall, Rb substitution deepens and stiffens the ferroelectric wells, reinforcing long-range order through enhanced electronic asymmetry rather than geometric strain. This chemically induced stabilization, together with the polarization enhancement in panels (b_1-b_3) and the charge asymmetry in Fig. 5, establishes Rb-doped $CsGeCl_3$ as the most robust and electronically clean ferroelectric in the series.

Panels (b_1)-(b_3) reveal the polarization evolution along the distortion path. The near-linear growth of $P(\lambda)$ for small λ reflects a strong piezo-polar coupling along the soft-mode eigenvector, with slope $(\partial P/\partial \lambda)_{\lambda \to 0}$ enhanced by Rb incorporation. This indicates that chemical pressure increases the piezoelectric susceptibility of the polar mode, an effect amplified in chlorides where bond compression stiffens the polar eigenvector and enhances lone-pair directionality. The saturation values at $\lambda = \pm 1$ define the spontaneous polarization, which grows with Rb substitution. Importantly, the polarization pathway is smooth and coherent, free of intermediate instabilities, confirming that chemical pressure strengthens rather than frustrates the ferroelectric order. Microscopically, this reflects stronger Ge *s*–X *p* hybridization, which shifts electronic charge density toward the polar axis. This mechanism aligns directly with the enhanced optical oscillator strengths observed in the excitonic spectra, demonstrating that ferroelectric distortions are inseparably tied to the strength of interband dipole transitions.

Panels (c_1) and (c_2) compare the spontaneous polarization P_s with tetragonality *c*/*a*. Although larger *c*/*a* ratios often accompany stronger polarization, the halogen dependence shows that structure alone does not dictate ferroelectric strength: iodides display larger *c*/*a* but smaller P_s than chlorides, emphasizing the dominant role of electronic asymmetry. Quantitatively, P_s decreases from 22.35 μC/cm^2 in $CsGeCl_3$ to 19.02 μC/cm^2 in $CsGeBr_3$ and 17.25 μC/cm^2 in $CsGeI_3$, following the reduction in Ge off-centering (0.35, 0.22, and 0.16 Å, respectively). This inverse correlation between P_s and *c*/*a* persists across exchange–correlation levels, with both mTASK and r2SCAN meta-GGAs reproducing the same hierarchy, confirming its robustness. To verify the Berry-phase (Bp) results, Born effective charges (BECs) combined with ionic displacements were used as an independent check, yielding lower absolute magnitudes (e.g., 10.86 μC/cm^2 for $CsGeCl_3$) because BECs capture only the ionic contribution, omitting electronic polarization. The consistency between Bp and BEC confirms that Ge *s*–X *p* charge redistribution is the main source of polarization. Experimentally, these trends agree with reported values of $\sim$15 μC/cm^2 for $CsGeBr_3$ single crystals[1] and 18–20 μC/cm^2 for $CsGeI_3$ thin films, where confinement and suppressed octahedral tilting enhance local off-centering. Although our 0 K first-principles P_s values slightly exceed the experimental measurements, the deviation lies within the expected range given the absence of thermal disorder, domain averaging, and finite-temperature dielectric screening in the calculations. This trend is consistent with prior theoretical and experimental reports on the strain and dimensional sensitivity of halide perovskites[50,51]; see also Table SM3. Overall, these results highlight that Rb substitution enhances P_s through reinforced lone-pair asymmetry and reduced dielectric screening rather than geometric strain, establishing chemical pressure as an electronically clean route to stabilize ferroelectricity.

These results satisfy the expected mathematical self-consistency. The curvature at $\lambda = 0$, $\kappa = \partial^2 \Delta E/\partial\lambda^2|_0 < 0$, reflects the unstable paraelectric state. The condition $P(\pm 1) = P_s$ matches the energy minima of $\Delta E(\lambda)$. The Rb-induced increase in $|\kappa|$ and P_s corresponds to a renormalization of the Landau coefficients, $\alpha \to \alpha'$ (more negative) and modestly increased β, yielding deeper yet stiffer wells. The halogen trend $P_s(\mathrm{Cl}) > P_s(\mathrm{Br}) > P_s(\mathrm{I})$ parallels the evolution of dielectric screening and exciton binding energies, since the internal field scales as $E_{\mathrm{int}} \sim P_s/\varepsilon$. Thus, ferroelectricity and excitonic behavior are revealed as two intertwined consequences of lone-pair activity and dielectric screening.

The integration of panels (a_i)-(c_j), for $i\ (j) = 1$ to $3\ (2)$, also points to practical design insights. Systems with deeper wells and larger P_s (notably $CsGeCl_3$ and $CsGeBr_3$) exhibit both stronger exciton binding and sharper BSE resonances (Fig. 2), offering advantages for light-emitting and exciton–polariton applications where stable polarization and strong radiative coupling are desired. In contrast, iodides, with shallower wells and weaker polarization, are predisposed to photovoltaic applications, where reduced E_b^{ex} and softer ferroelectric barriers facilitate charge separation and bulk-photovoltaic effects. Rb substitution fortifies ferroelectric stability across all halides without compromising band-edge purity, enabling simultaneous control of polarization retention and optical response.

Most importantly, the link between the ferroelectric energy landscape and excitonic behavior reveals a novel co-design pathway. Chemical pressure not only deepens $\Delta E_{\mathrm{barrier}}$ and strengthens P_s, but also sharpens excitonic resonances by reducing dielectric screening. This dual tuning confirms that ferroelectric stability and many-body optics share a common microscopic origin in Ge lone-pair localization and Ge–X orbital hybridization. Practically, this means that by adjusting composition (Cl/Br vs. I, with or without Rb) and strain, one can continuously navigate between two regimes: robust ferroelectrics with stable excitons for memories and LEDs, and softer photoferroelectrics with weakly bound excitons for shift-current photovoltaics.

In sum, Figure 4 establishes chemical pressure as a clean and versatile design lever that unifies lattice energetics, spontaneous polarization, and excitonic response. The ability to link $\Delta E(\lambda)$, $P(\lambda)$, and $(P_s,\ c/a)$ to dielectric screening and optical properties provides a predictive, quantitatively consistent framework for engineering lead-free halide perovskites across optoelectronic and ferroic applications. The novel finding here is that Rb substitution enhances not just polarization stability but also light-matter coupling through a shared electronic mechanism, completing a closed design loop between ferroelectricity and excitonics.

Quantifying chemical pressure induced by Rb substitution

Throughout this work, partial substitution of Cs by Rb is referred to as *chemical pressure*, reflecting the internal strain and stress generated by ionic-size mismatch rather than macroscopic volume compression. To make this concept explicit and quantitative, we analyze the lattice strain induced by Rb incorporation, evaluate the corresponding internal stress using linear elasticity theory, and map it onto an equivalent hydrostatic pressure scale for direct comparison with externally applied pressure.

Importantly, as shown below, Rb substitution produces only very small volumetric changes ($\lesssim 0.2\%$). The dominant effect of chemical substitution therefore arises from anisotropic internal stresses rather than uniform lattice contraction, clarifying the physical meaning and limitations of the chemical-pressure analogy.

Elastic properties of pristine $CsGeX_3$

The elastic response of pristine $CsGeX_3$ (X = Cl, Br, I) provides the reference required to convert substitution-induced strain into internal stress. Elastic constants C_{ij} were computed from first principles using IRelast code[53] for the rhombohedral ground state and expressed in the hexagonal setting, which allows a transparent separation of in-plane (*a*) and polar-axis (*c*) responses.

Table 2 lists the individual elastic constants together with selected linear combinations entering the stress–strain relations under axial and volumetric deformations. These combinations are reported explicitly to enable direct evaluation of anisotropic stress components without additional fitting parameters.

Across the halide series, the elastic constants decrease systematically from Cl to I, reflecting progressive lattice softening driven by increasing anion size and polarizability. In particular, the marked reduction of the shear modulus C_{44} highlights the enhanced structural flexibility of iodides, consistent with their larger dielectric response and reduced resistance to polar distortions. This elastic softening underpins the strong sensitivity of excitonic and dielectric properties to even weak lattice perturbations discussed in Figs. 1 and 2.

Strain, stress, and effective chemical pressure

Rb substitution induces anisotropic lattice distortions, which we quantify through the axial strains

$$\varepsilon_a = \frac{a_{\mathrm{Rb}} - a_0}{a_0}, \qquad \varepsilon_c = \frac{c_{\mathrm{Rb}} - c_0}{c_0}, \tag{2}$$

Elastic Constant	$CsGeCl_3$	$CsGeBr_3$	$CsGeI_3$
C_{11}	40.45	33.71	40.29
C_{33}	25.65	26.65	22.60
C_{44}	14.53	13.19	10.70
C_{12}	11.95	15.06	0.28
C_{13}	16.88	15.78	9.60
$C_{11} + C_{12}$	52.40	48.77	40.57
$C_{11} + C_{33} + 2C_{13}$	99.85	91.93	82.08

Table 2. Elastic constants C_{ij} (in GPa) of pristine $CsGeX_3$ (X = Cl, Br, I) perovskites in the hexagonal setting. Individual constants are followed by combinations relevant for axial and volumetric stress evaluation within linear elasticity theory.

Compound	ε_a	ε_c	$\sigma_{xx} = \sigma_{yy}$	σ_{zz}	P_{eff}
$CsGeCl_3$	0.042	0.300	0.072	0.091	-0.078
$CsGeBr_3$	-0.075	0.349	0.019	0.069	-0.036
$CsGeI_3$	0.071	0.396	0.067	0.103	-0.079

Table 3. Axial strains (ε_a and ε_c in %), internal stress components ($\sigma_{xx} = \sigma_{yy}$ and σ_{zz} in GPa), and effective chemical pressure (P_{eff} in GPa) induced by Rb substitution in $CsGeX_3$ (X = Cl, Br, I) perovskites. Positive stress corresponds to compression; negative P_{eff} indicates tensile chemical pressure.

and the volumetric strain

$$\varepsilon_V = \frac{V_{\text{Rb}} - V_0}{V_0}, \tag{3}$$

where a_0, c_0, and V_0 refer to the pristine lattice.

Using linear elasticity in the hexagonal representation, the internal stress components are given by

$$\sigma_{xx} = (C_{11} + C_{12})\,\varepsilon_a + C_{13}\,\varepsilon_c, \tag{4}$$

$$\sigma_{yy} = \sigma_{xx}, \tag{5}$$

$$\sigma_{zz} = 2C_{13}\,\varepsilon_a + C_{33}\,\varepsilon_c. \tag{6}$$

To enable direct comparison with externally applied hydrostatic pressure, we define an effective chemical pressure as

$$P_{\text{eff}} = -\frac{1}{3}\left(\sigma_{xx} + \sigma_{yy} + \sigma_{zz}\right). \tag{7}$$

The resulting axial strains, stress components, and effective pressures are summarized in Table 3. In all cases, the extracted effective pressures are small in magnitude ($|P_{\text{eff}}| < 0.1$ GPa) and negative, indicating that Rb substitution induces a weak tensile chemical pressure associated with slight lattice expansion rather than compression.

Crucially, the stress tensor is strongly anisotropic, with $\sigma_{zz} > \sigma_{xx} = \sigma_{yy}$ across the halide series. This demonstrates that chemical pressure primarily couples to the polar *c*-axis, in contrast to ideal hydrostatic compression where the stress state is isotropic and the axial ratio remains fixed. As a result, chemical pressure and hydrostatic pressure are not strictly equivalent perturbations, even though they can produce qualitatively similar trends in band gaps, dielectric screening, and exciton binding energies.

The small magnitude of P_{eff} does not contradict the pronounced excitonic and dielectric effects observed upon Rb substitution. $CsGeX_3$ perovskites lie close to polar and ferroelectric instabilities, where dielectric screening, band-edge dispersion, and exciton binding energies are exceptionally sensitive to weak, directionally selective lattice perturbations. Consequently, modest substitution-induced anisotropic stresses can generate optical responses comparable to those achieved under several gigapascals of external hydrostatic pressure, as demonstrated by the systematic trends reported in Figs. 1 and 2.

This analysis establishes a clear and quantitative framework for comparing chemical and mechanical tuning mechanisms, while highlighting their fundamental physical differences.

Electronic bonding, charge redistribution, and lone-pair localization as the microscopic origin of ferroelectricity in $CsGeX_3$ perovskites

Figure 5 integrates charge-transfer metrics, real-space electron localization, and macroscopic polarization to reveal the microscopic origin of ferroelectricity in $CsGeX_3$ perovskites and their Rb-alloys. The analysis builds directly on the formalism outlined in "Quantifying charge transfer via Bader analysis", where Bader charges q_i are obtained from all-electron densities by partitioning the system into atomic basins, with deviations $|\Delta q_i|$ [Eq. (28)] quantifying covalency and charge redistribution. Stoichiometric neutrality SN [Eq. (29)] serves as an internal consistency check, ensuring that observed asymmetries reflect genuine bonding effects. Complementarily, the ELF maps introduced in "Bonding Visualization via the Electron Localization Function" provide a spatial measure of Pauli-limited localization, with the normalized lone-pair index η_{lp} [Eq. (31)] serving as a quantitative descriptor of stereochemical activity.

The Bader charges in panel (a) confirm that the A-site cations (Cs, Rb) retain nearly ideal +1e character, underlining their spectator role in electronic transport and polarization. By contrast, the Ge and halogen sites exhibit marked deviations from nominal valences, as summarized in panel (b). Across the Cl–Br–I sequence, halogen charges become progressively less negative, while $|\Delta q_X|$ increases, pointing to enhanced Ge–X covalency and orbital delocalization. The Ge site mirrors this progression, with its charge decreasing from about 1.07*e* in $CsGeCl_3$ to 0.65*e* in $CsGeI_3$. Importantly, all systems satisfy stoichiometric neutralization within numerical accuracy, excluding spurious leakage and underscoring that these variations stem from redistribution within the crystal. Rb substitution deepens this effect modestly, decreasing $|\Delta q_{\mathrm{Ge}}|$ while leaving the stoichiometric neutralization (SN) nearly unchanged, indicating a slight shift toward a more ionic bonding character without charge imbalance. This electronic fingerprint reveals the action of chemical pressure: the smaller Rb^+ ion contracts the lattice, amplifying Ge–X overlap and enhancing polarizability without generating mid-gap states or defect levels.

Panels (c_i) and (d) recast these charge-transfer results into a direct picture of lone-pair activity through the ELF. In $CsGeCl_3$, Ge-centered ELF lobes are sharply localized, reflecting a strongly stereochemically active $4s^2$ lone pair. This localization weakens in $CsGeBr_3$ and becomes increasingly diffuse in $CsGeI_3$, a trend captured quantitatively by the lone-pair localization index η_{lp}, which decreases from 0.264 (Cl) to 0.259 (Br) to 0.225 (I). For further details, see Secs. SM7 and SM9, as well as Listing 4. The same trend is mirrored in the spontaneous polarization $\boldsymbol{P}_s$ extracted from Berry-phase theory [Eqs. (26) and (27)]—22.35, 19.02, and 17.25 $\mu\mathrm{C/cm}^2$ for Cl, Br, and I respectively—yet anticorrelates with tetragonality *c*/*a*, which increases from 1.244 to 1.277 across the series. This decoupling is a central finding: ferroelectricity is not dictated by geometric elongation alone, but by electronic asymmetry driven by lone-pair localization. Chemically, the progression from Cl to I reduces halogen electronegativity and increases orbital diffuseness, delocalizing the Ge lone pair and lowering η_{lp}. Rb substitution reverses this dilution, compressing the Ge–X framework, sharpening the ELF lobes, and reinforcing polar instability, consistent with the deeper double wells and steeper $P(\lambda)$ slopes observed in Fig. 4.

The connection to excitonic physics becomes evident when comparing with Fig. 2. Large η_{lp} values, characteristic of chlorides, correspond to reduced static screening $\varepsilon(0)$, stronger localization of band-edge states, and larger exciton binding energies E_b^{ex}, in line with the hydrogenic dependence $E_b^{\mathrm{ex}} \propto \mu/\varepsilon^2$ [Eq. (25)]. Conversely, smaller η_{lp} in iodides corresponds to higher $\varepsilon(0)$, smaller μ, weaker excitonic redshifts, and a softer dielectric response, consistent with the ELOSS blueshifts in Fig. 1. Chlorides are therefore uniquely responsive to chemical pressure, as their initially large η_{lp} and small *c*/*a* allow modest Rb substitution to substantially increase both P_s and E_b^{ex} without incurring high elastic energy costs. In iodides, where η_{lp} is already small and *c*/*a* large, the same substitution pushes the system toward photovoltaic-friendly regimes dominated by free-carrier generation and reduced excitonic confinement.

To ensure that the lone-pair localization index η_{lp} is a robust and physically meaningful descriptor rather than an artifact of visualization choices, we systematically tested its stability with respect to (i) ELF threshold selection, (ii) choice of crystallographic slicing plane, and (iii) image-segmentation procedure. Across all tested conditions, the relative ordering $\eta_{\mathrm{lp}}(\mathrm{Cl}) > \eta_{\mathrm{lp}}(\mathrm{Br}) > \eta_{\mathrm{lp}}(\mathrm{I})$ remains unchanged, and absolute variations remain within a narrow numerical window that does not affect the observed correlations with spontaneous polarization $\boldsymbol{P}_s$ or exciton binding energy E_b^{ex}. This insensitivity reflects the fact that η_{lp} captures an integrated geometric property of the Ge-centered ELF topology, rather than a single contour level. Detailed sensitivity analyses and methodological validation are provided in "Robustness and Validation of the Lone-Pair Localization Index", confirming that η_{lp} is a transferable and threshold-independent measure of stereochemically active lone-pair localization.

Together, these results establish Bader charge deviations $|\Delta q_i|$, ELF-derived lone-pair localization indices η_{lp}, and Berry-phase polarization P_s as interconnected descriptors of the same underlying mechanism: the stereochemical activity of the Ge(II) $4s^2$ lone pair. By tuning this mechanism through chemical pressure or strain, one can continuously manipulate charge redistribution, lone-pair localization, dielectric screening, and exciton binding, thereby steering materials between regimes of robust ferroelectric exciton retention, suited for memories and polaritonics, and soft photoferroelectrics optimized for bulk-photovoltaic effects. In this sense, Fig. 5 shows that lone-pair localization is not merely a qualitative motif but a quantitative, transferable design parameter for co-engineering ferroic and optical functionalities in lead-free halide perovskites. Additional details are provided in "SM11C", Tables SM4 and SM5, and Fig. SM14.

Conclusion

We have established a unified microscopic framework that connects excitonic renormalization, dielectric screening, and ferroelectric stability in lead-free $CsGeX_3$ halide perovskites. By combining GW+BSE many-body spectroscopy, Berry-phase polarization, Bader charge analysis, and ELF-based lone-pair quantification, we identify the stereochemical activity of the Ge(II) $4s^2$ lone pair as the common origin of both optical and ferroic responses. The normalized lone-pair localization index, extracted from real-space ELF maps, emerges as a quantitative and transferable descriptor that governs exciton binding, dielectric anisotropy, and spontaneous polarization. This elevates lone-pair localization from a qualitative concept to a predictive design parameter.

Two experimentally accessible levers—A-site substitution and hydrostatic compression—enable systematic control of this coupled exciton–ferroelectric landscape. Rb substitution acts as clean chemical pressure, compressing the Ge–X framework, deepening the ferroelectric double-well, enhancing spontaneous polarization, and sharpening excitonic resonances by suppressing dielectric screening. Hydrostatic compression exerts the complementary effect, delocalizing band-edge states, reducing exciton binding, and softening the ferroelectric barrier. Together, these results demonstrate that excitonic and ferroic properties can be co-designed through the same underlying electronic asymmetry, providing access to regimes ranging from strong exciton retention with robust polarization to weakly bound excitons with facile switching.

This framework translates directly into design rules for multifunctional devices. Chloride- and bromide-rich compositions, especially with modest Rb alloying, combine large polarization, deeply bound excitons, and suppressed dielectric loss—an ideal profile for polarization-assisted emitters, exciton–polariton condensates, and non-volatile ferroelectric memories. Iodide-rich compounds, by contrast, exhibit softer wells and weaker exciton binding, naturally suited for ferroelectric photovoltaics and bulk-photovoltaic operation where efficient carrier separation dominates. The ability to tune exciton binding independently of dielectric dissipation through chemical pressure and strain establishes a versatile platform for integrated optoelectronic–ferroic architectures.

Looking ahead, epitaxial strain and heterostructure engineering offer complementary pathways to modulate lone-pair localization without chemical substitution. Time-resolved and nonlinear optical probes could provide direct spectroscopic evidence of the predicted coupling between excitonic resonances and ferroelectric switching. Moreover, the concept of lone-pair driven co-design extends beyond Ge-based perovskites to other lead-free families with stereochemically active cations such as Bi and Sn, expanding the palette of environmentally benign multifunctional materials.

In summary, by unifying excitonic and ferroelectric control through the common mechanism of lone-pair localization, we provide a coherent and predictive strategy for designing lead-free halide perovskites. Chemical pressure and strain emerge as powerful, experimentally viable tools to co-optimize light–matter coupling, exciton stability, and ferroelectric robustness within a single material platform, advancing the vision of high-performance, multifunctional, and sustainable perovskite optoelectronics.

Theory and methods

To characterize the optoelectronic and ferroic properties of halide perovskites, we employ four complementary first-principles approaches: (i) many-body perturbation theory (MBPT) via the Green's function (GW) approximation[54,55] and the Bethe–Salpeter equation (BSE)[56–59] for quasiparticle and excitonic properties ("Many-body perturbation theory for optical excitations"); (ii) the Berry phase formalism for computing spontaneous polarization from ionic and electronic contributions ("Quantifying spontaneous polarization via the berry phase formalism"); (iii) quantifying charge transfer via Bader charge analysis ("Quantifying charge transfer via Bader analysis"); and (iv) the electron localization function (ELF) to visualize bonding and lone-pair localization ("Bonding visualization via the electron localization function").

Many-Body Perturbation Theory for Optical Excitations

To model the optical response of halide perovskites with strong excitonic effects and weak screening, we apply MBPT via GW and BSE, which improve on density functional theory (DFT) by including quasiparticle (QP) corrections and exciton binding. In Fig. 6, DFT + RPA treats optical transitions as vertical excitations between KS states[36], omitting QP shifts and electron–hole interactions. DFT + G_0W_0 + RPA introduces the self-energy $\Sigma = iGW$[54,55,60], replacing V_{XC} with a nonlocal potential, and yields corrected QP energies[57]:

$$\epsilon_{n\mathbf{k}}^{\mathrm{QP}} = \epsilon_{n\mathbf{k}}^{\mathrm{KS}} + \langle \psi_{n\mathbf{k}} | \Sigma(\epsilon_{n\mathbf{k}}^{\mathrm{QP}}) - V_{\mathrm{XC}} | \psi_{n\mathbf{k}} \rangle, \tag{8}$$

where $\psi_{n\mathbf{k}}$ is the Kohn-Sham (KS) wavefunction. However, only DFT + GW + BSE (right panel of Fig. 6) includes screened electron–hole attraction, capturing bound excitons and sub-gap absorption features.

The BSE models neutral excitations using correlated two-particle states $|A_\lambda\rangle$ with excitation energies E_λ, obtained by solving[57,61]:

$$H^{(\mathrm{eff})} |A_\lambda\rangle = E_\lambda |A_\lambda\rangle, \tag{9}$$

where the Hamiltonian is

$$H^{(\mathrm{eff})} = H^{(\mathrm{diag})} + 2\gamma_{\mathrm{x}} H^{(\mathrm{x})} + \gamma_{\mathrm{c}} H^{(\mathrm{c})}, \tag{10}$$

and $H^{(\mathrm{diag})}$ contains QP transition energies:

$$H_{\alpha\beta}^{(\mathrm{diag})} = \left(\epsilon_{c_\alpha \mathbf{k}_\alpha}^{\mathrm{QP}} - \epsilon_{v_\alpha \mathbf{k}_\alpha}^{\mathrm{QP}} \right) \delta_{\alpha\beta}. \tag{11}$$

The BSE hierarchy begins with the independent-particle (IP) limit using only $H^{(\mathrm{diag})}$[62], omitting electron–hole interactions[57]. Adding $H^{(\mathrm{x})}$ yields the random phase approximation (RPA), capturing exchange and local-field effects, while $H^{(\mathrm{c})}$ introduces screened Coulomb attraction—crucial for excitons and dominant in spin-triplet

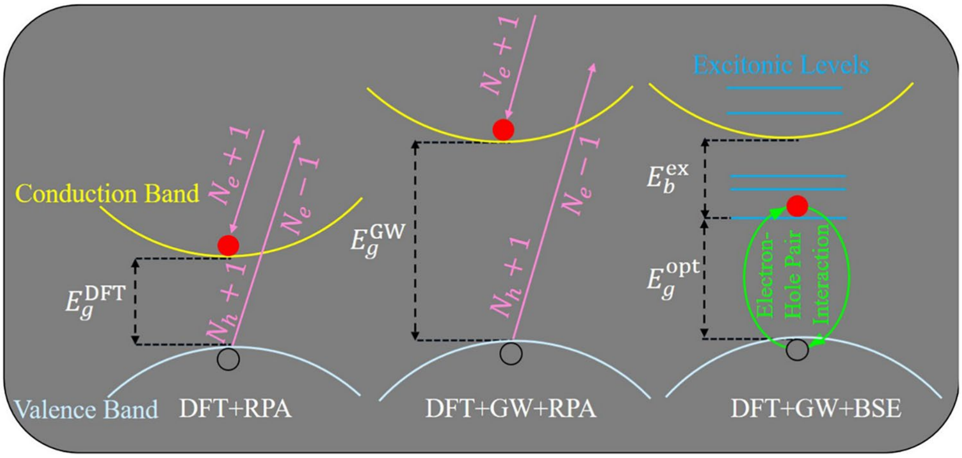

Fig. 6. Three levels of theory for optical excitations. Left: DFT+RPA shows vertical interband transitions without QP or excitonic effects. Middle: GW adds QP corrections, improving gap accuracy but neglecting electron–hole interactions. Right: GW+BSE includes screened electron–hole attraction, forming bound excitons and sub-gap absorption, critical for low-screening materials like halide perovskites. Each step adds essential physics for accurate optical spectra.

states where $H^{(\mathrm{x})}$ vanishes. The full BSE, with all terms[58], captures bound excitons and sub-gap absorption in materials like halide perovskites. We define "RPA" as including $H^{(\mathrm{x})}$ only, and "BSE" as the full singlet form; see Ref.[63], pp. 20–21.

The exchange term $H^{(\mathrm{x})}_{\alpha\beta}$, enforcing fermionic antisymmetry via the bare Coulomb potential $v(\mathrm{r}_e, \mathrm{r}_h) = 1/|\mathrm{r}_e - \mathrm{r}_h|$, is given by[57,61]:

$$H^{(\mathrm{x})}_{\alpha\beta}(\mathrm{q}) = \iint \Phi^{(r)*}_{\alpha}(\mathrm{r}_e, \mathrm{r}_e)\, v(\mathrm{r}_e, \mathrm{r}_h)\, \Phi^{(r)}_{\beta}(\mathrm{r}_h, \mathrm{r}_h)\, d^3 r_e\, d^3 r_h, \tag{12}$$

where $\Phi^{(r)}$ is the resonant two-particle wavefunction. The direct term $H^{(\mathrm{c})}$ accounts for screened electron–hole attraction[57,61]:

$$H^{(\mathrm{c})}_{\alpha\beta}(\mathrm{q}) = -\iint \Phi^{(r)*}_{\alpha}(\mathrm{r}_e, \mathrm{r}_h)\, W(\mathrm{r}_e, \mathrm{r}_h)\, \Phi^{(r)}_{\beta}(\mathrm{r}_e, \mathrm{r}_h)\, d^3 r_e\, d^3 r_h, \tag{13}$$

with

$$W(\mathrm{r}_e, \mathrm{r}_h) = \int v(\mathrm{r}_e, \mathrm{r})\, \varepsilon^{-1}(\mathrm{r}, \mathrm{r}_h)\, d^3 r, \tag{14}$$

where ε^{-1} is the inverse dielectric function describing screening.

The BSE Hamiltonian can be block-decomposed into resonant and anti-resonant sectors[64]:

$$H^{(\mathrm{eff})} = \begin{pmatrix} H^{\mathrm{rr}} & H^{\mathrm{ra}} \\ H^{\mathrm{ar}} & H^{\mathrm{aa}} \end{pmatrix}, \tag{15}$$

with each block containing contributions from $H^{(\mathrm{diag})}$, $H^{(\mathrm{x})}$, and $H^{(\mathrm{c})}$ (10). The off-diagonal terms H^{ra}, H^{ar} couple excitation and de-excitation channels. Neglecting them defines the Tamm–Dancoff approximation (TDA), which simplifies the eigenvalue problem[64]:

$$H^{(\mathrm{eff})} \begin{pmatrix} X^{\lambda} \\ Y^{\lambda} \end{pmatrix} = E_{\lambda} \begin{pmatrix} X^{\lambda} \\ Y^{\lambda} \end{pmatrix}, \tag{16}$$

where X^{λ} and Y^{λ} are expansion coefficients of the exciton wavefunction. The resonant and anti-resonant basis functions are

$$\Phi^{(\mathrm{r})}_{\alpha} = \psi_{v_\alpha \mathrm{k}^+_\alpha}(\mathrm{r}_h)\, \psi^*_{c_\alpha \mathrm{k}^-_\alpha}(\mathrm{r}_e), \quad \Phi^{(\mathrm{a})}_{\alpha} = \psi_{c_\alpha \mathrm{k}^+_\alpha}(\mathrm{r}_e)\, \psi^*_{v_\alpha \mathrm{k}^-_\alpha}(\mathrm{r}_h), \tag{17}$$

with $\mathrm{k}^{\pm}_{\alpha} = \mathrm{k}_{\alpha} \pm \mathrm{q}/2$. In the optical limit ($\mathrm{q} = 0$), transitions become vertical, and TDA retains only H^{rr}:

$$H^{(\mathrm{eff})}_{\mathrm{TDA}} = H^{\mathrm{rr}}, \tag{18}$$

reducing computational cost while preserving exciton accuracy near the band edge.

In the optical limit ($q \to 0$), the imaginary part of the macroscopic dielectric function $\Im[\varepsilon_M^{\mu\nu}(\omega)]$ governs absorption and is computed from BSE eigenstates[57,61]:

$$\Im[\varepsilon_M^{\mu\nu}(\omega)] = \frac{4\pi^2}{V} \sum_{\lambda} t^*_{\lambda,\mu} t_{\lambda,\nu} \frac{1}{\pi\delta} \left(\frac{\delta^2}{(\omega - E_\lambda)^2 + \delta^2} - \frac{\delta^2}{(\omega + E_\lambda)^2 + \delta^2} \right), \tag{19}$$

where E_λ is the exciton energy, δ is a broadening parameter, and $t_{\lambda,\mu}$ is the dipole transition strength in direction μ, given in TDA by:

$$t_{\lambda,\mu} = i \sum_{\alpha} X_\alpha^\lambda \langle c_\alpha \mathrm{k}_\alpha | \hat{r}_\mu | v_\alpha \mathrm{k}_\alpha \rangle, \tag{20}$$

with X_α^λ the excitonic amplitude for transition $\alpha = (v_\alpha, c_\alpha, \mathrm{k}_\alpha)$. Beyond TDA, both X_α^λ and Y_α^λ contribute[57,61]:

$$t^*_{\lambda,\mu} = i \sum_{\alpha} (X_\alpha^\lambda + Y_\alpha^\lambda) \langle c_\alpha \mathrm{k}_\alpha | \hat{r}_\mu | v_\alpha \mathrm{k}_\alpha \rangle. \tag{21}$$

The Lorentzian in Eq. (19) models broadening, and the oscillator strength scales with $|t_{\lambda,\mu}|^2$. Since $\hat{\mathrm{r}}$ is ill-defined in periodic systems, the dipole matrix element is rewritten using the momentum operator:

$$\langle c | \hat{r}_\mu | v \rangle = \frac{1}{i m_e (\epsilon_c - \epsilon_v)} \langle c | \hat{p}_\mu | v \rangle, \tag{22}$$

derived from $[\hat{H}, \hat{r}_\mu] = \frac{i\hbar}{m_e} \hat{p}_\mu$ using $\hat{H}|n\rangle = \epsilon_n |n\rangle$ and atomic units ($\hbar = 1$).

In Eq. (12), $\Phi_\alpha^{(r)*}(\mathrm{r}_e, \mathrm{r}_e)$ and $\Phi_\beta^{(r)}(\mathrm{r}_h, \mathrm{r}_h)$ show that exchange acts only when electron and hole coincide, enforcing Pauli exclusion, yielding repulsion and local-field effects. This term vanishes in spin-triplet states ($\gamma_\mathrm{x} = 0$), while both exchange and correlation contribute for spin-singlets ($\gamma_\mathrm{x} = \gamma_\mathrm{c} = 1$), as in Eq. (10). The exciton binding energy is

$$E_b^{\mathrm{ex}} = E_g^{\mathrm{GW}} - E_g^{\mathrm{opt}}, \tag{23}$$

where E_g^{GW} is the QP gap and E_g^{opt} the lowest bright exciton energy, with E_b^{ex} marking the separation between QP continuum and excitonic states (Fig. 6). A hydrogenic estimate gives

$$E_b^{\mathrm{hydro}} = \frac{\mu e^4}{2(4\pi\varepsilon_0\varepsilon_r)^2\hbar^2}. \tag{24}$$

Here, μ is the reduced effective mass, ε_0 denotes the vacuum permittivity, while ε_r is the relative dielectric constant of the material. In atomic units, $4\pi\varepsilon_0 = 1$, so that $\varepsilon \equiv \varepsilon_r$. While this model neglects screening anisotropy and band dispersion, it motivates the scaling

$$E_b^{\mathrm{ex}} \propto \frac{\mu}{\varepsilon^2(0)}, \tag{25}$$

used in Secs. "Exciton–plasmon coevolution under chemical pressure and hydrostatic strain", "Orbital control of excitons, screening, and ferroelectricity: insights from the projected DOS", and "Electronic Bonding, Charge Redistribution, and Lone-Pair Localization as the Microscopic Origin of Ferroelectricity in $CsGeX_3$ Perovskites" to analyze trends across materials, where $\varepsilon(0)$ is the zero-frequency dielectric response.

Role of dielectric screening and lattice polarization in exciton binding

In ferroelectric materials, the static dielectric constant $\varepsilon(0)$ (i.e., the zero-frequency dielectric response including both electronic and lattice contributions) can be strongly enhanced by soft polar phonons associated with lattice instabilities. In principle, the lattice contribution may substantially reduce exciton binding energies by increasing long-range Coulomb screening. It is therefore important to clarify which dielectric contributions are included in the present many-body calculations and how this choice affects the interpretation of excitonic stability in $CsGeX_3$ perovskites.

To avoid confusion, we note that ε_0 in Eq. (24) refers to the vacuum permittivity, whereas throughout this work $\varepsilon(0)$ denotes the dimensionless material's static dielectric constant.

In this work, excitonic properties are computed within the standard G_0W_0+BSE framework, where the screened electron–hole interaction is constructed using the *electronic* dielectric function ε_∞, evaluated within the RPA. In the present G_0W_0+BSE calculations, screening is constructed from the electronic dielectric constant ε_∞, while lattice (ionic or phononic) contributions, $\varepsilon_{\mathrm{lattice}}$, entering $\varepsilon(0)$ are not explicitly included, *viz.* $\varepsilon(0) = \varepsilon_\infty + \varepsilon_{\mathrm{lattice}} \approx \varepsilon_\infty$. This treatment is physically appropriate for optical absorption processes, which correspond to vertical electronic excitations occurring on ultrafast timescales, well before ionic degrees of freedom can respond. As a result, both the calculated spectra and the extracted exciton binding energies correspond to the electronic screening limit probed in optical experiments.

The exclusion of lattice polarization implies that the calculated exciton binding energies represent an upper bound with respect to the fully screened (static) interaction. In a complete dynamical picture, coupling to soft polar phonons would further renormalize the Coulomb interaction and partially reduce E_b^{ex}. Importantly, however, such phonon-mediated screening acts in a largely uniform manner within a given structural phase and does not alter the *relative* trends reported here. All compounds are treated consistently at the same theoretical level, ensuring that comparisons across halogen chemistry, Rb-induced chemical pressure, and hydrostatic strain remain meaningful.

This interpretation is supported by the strong correlation established between exciton binding energies, the electronic dielectric constant ε_∞, and the lone-pair localization index η_{lp} (Figs. 2 and 5). Materials with strongly localized Ge $4s^2$ lone pairs exhibit reduced electronic screening and enhanced excitonic confinement, whereas heavier halides show increased electronic delocalization, larger ε_∞, and weaker exciton binding. Lattice polarization therefore modulates excitonic stability but does not overturn the electronic-structure-driven trends identified in this work.

We emphasize that the central conclusions of the manuscript concern the *shared electronic origin* of ferroelectricity and excitonic behavior, rooted in lone-pair–induced charge asymmetry. These conclusions remain valid irrespective of whether lattice contributions are included explicitly, as they arise from changes in electronic structure rather than from phonon softening alone. A full treatment of exciton–phonon coupling and finite-temperature dielectric renormalization represents an important direction for future work, but lies beyond the scope of the present study.

Quantifying spontaneous polarization via the berry phase formalism

Spontaneous polarization in ferroelectrics arises from inversion-symmetry-breaking distortions and is computed via DFT using the mTASK functional[65] and `VX_HCTH407` potential[66]. The total polarization $\boldsymbol{P}^{(\lambda)}$ includes ionic and Berry-phase electronic terms:

$$\begin{aligned}\boldsymbol{P}^{(\lambda)} &= \frac{e}{\Omega^{(\lambda)}} \sum_{s=1}^{N} Z_s^{\mathrm{ion}(\lambda)} \mathrm{r}_s^{(\lambda)} \\ &+ \frac{2e}{(2\pi)^3} \sum_{n=1}^{M} \int_{1\mathrm{BZ}^{(\lambda)}} d\mathrm{k}\, \langle u_{n\mathrm{k}}^{(\lambda)} | -i\nabla_{\mathrm{k}} | u_{n\mathrm{k}}^{(\lambda)} \rangle,\end{aligned} \tag{26}$$

and the spontaneous polarization is the difference between polar and centrosymmetric phases:

$$\boldsymbol{P}_s = \boldsymbol{P}^{(1)} - \boldsymbol{P}^{(0)}. \tag{27}$$

This modern theory[67–71] ensures gauge-invariant polarization in periodic systems; see also Refs.[63,72].

Quantifying charge transfer via Bader analysis

Bader analysis, based on QTAIM[73,74], partitions the electron density $\rho(\mathrm{r})$ into atomic basins Ω_i via zero-flux surfaces satisfying: $\nabla\rho(\mathrm{r}) \cdot \hat{n}(\mathrm{r}) = 0$, where $\hat{n}(\mathrm{r})$ is the surface normal. The Bader charge q_i of atom *i* is: $q_i = \int_{\Omega_i} \rho(\mathrm{r})\, d\mathrm{r}$, and its deviation from the nominal oxidation state defines the charge transfer:

$$|\Delta q_i| = |q_i^{\mathrm{crystal}} - q_i^{\mathrm{nominal}}|. \tag{28}$$

Larger $|\Delta q_i|$ indicates stronger covalency; we use nominal charges of +1*e* (Cs, Rb), +2*e* (Ge), and −1*e* (Cl, Br, I). Charge conservation is checked by

$$\mathrm{SN} = \sum_i q_i - N_e, \tag{29}$$

with N_e the stoichiometric electron count. All-electron charge densities were obtained via WIEN2k[35,36] and post-processed using Critic2[75,76]; for more on topological features, see Refs.[77,78].

Bonding visualization via the electron localization function

To visualize bonding and electron pairing in halide perovskites, we compute the electron localization function (ELF)[79], which measures the likelihood of finding a same-spin electron near another. ELF values near 1 signal strong localization (e.g., covalent bonds, lone pairs), while values around 0.5 indicate delocalized or metallic states. The ELF is defined as

$$\mathrm{ELF}(\mathrm{r}) = \frac{1}{1+\chi(\mathrm{r})}, \tag{30}$$

with localization index $\chi(\mathrm{r}) = \frac{D(\mathrm{r})}{D_h(\mathrm{r})}$, where $D_h(\mathrm{r})$ is the kinetic energy density of a homogeneous electron gas, and $D(\mathrm{r}) = \frac{1}{2}\sum_i |\nabla\psi_i(\mathrm{r})|^2 - \frac{1}{8}\frac{|\nabla\rho(\mathrm{r})|^2}{\rho(\mathrm{r})}$, is the Pauli excess kinetic energy density based on the KS orbitals ψ_i and electron density $\rho(\mathrm{r})$. ELF thus provides chemically intuitive maps of bonding and lone pairs, especially useful in polar or distorted perovskites.

Computational details

We computed the QP band structure and excitonic response of Rb-doped $CsGeX_3$ (X = Cl, Br, I) using the all-electron FP-LAPW method in EXCITING[80,81], which treats core–valence interactions without pseudopotentials. KS states were obtained via GGA-PBE[82] ($3 \times 3 \times 1$ k-mesh, rgkmax $= 7.0$, gmaxvr $= 14$); QP corrections were applied using single-shot G_0W_0[55] with $\Sigma = iGW$ on a $2 \times 2 \times 1$ grid, rgkmax $= 5.0$, gmaxvr $= 12$, and 30 empty bands to build GW [Eq. (8)], see Fig. SM2. The BSE was solved in the TDA[64] using $H^{(\mathrm{eff})}$ [Eq. (10)] with $H^{(\mathrm{diag})}$, $H^{(\mathrm{x})}$ [Eq. (12)], and $H^{(\mathrm{c})}$ [Eq. (13)]. We included 6 valence and 6 conduction bands (`nstlbse = "157 162 1 6"`), extended to 50 valence bands for continuum (`nstlbse = "109 162 1 6"`) for $CsGeCl_3$, sampled over a $6 \times 6 \times 2$ grid to converge E_b^{ex} [Eq. (23)]. Absorption spectra were obtained via Eq. (19) using $\delta = 0.007$ Ha on a 0–1 Ha, 1200-point mesh; RPA spectra (with $H^{(\mathrm{x})}$ only) and dipole matrix elements from Eqs. (20), (22) ensured gauge invariance.

Elastic behavior characterizes the reversible response of solids to applied stress, whereby internal forces restore the equilibrium configuration once the external load is removed[83,84]. This response is quantitatively described by the elastic constants, which play a central role in governing phase stability, lattice vibrational properties, and thermodynamic behavior of crystalline materials[85–90]. In the present work, elastic constants are computed using the energy–strain formalism as implemented in the IRELAST code[53], interfaced with the WIEN2K package[91]. IRELAST extends the earlier CUBICEELAST framework[92] to treat arbitrary crystal symmetries and has been extensively validated against experimental measurements and first-principles benchmarks across a wide range of materials[88,93–95].

Ferroelectric polarization was calculated using FP-(L)APW+lo in WIEN2K[35,36,91] with both PBE[82] and SCAN[65], the latter improving $\boldsymbol{P}_s$ predicted via the Berry-phase formalism[67–71], as expressed in Eqs. (26)] and (27), using $R_{\mathrm{MT}}K_{\max} = 7.0$, 14 Bohr^{-1} cutoff, and ∼2000 k-points. ELF maps[79] ("Bonding Visualization via the Electron Localization Function") were post-processed using a Python-based OpenCV pipeline employing HSV segmentation (Hue: 120–160), morphological filtering, and composition-wise partitioning ("SM7" and Listing 4) to compute the lone-pair localization index:

$$\eta_{\mathrm{lp}} = A_{\mathrm{lp}}/A_{\mathrm{ELF}}, \tag{31}$$

which correlates with $\boldsymbol{P}_s$ ("Quantifying Spontaneous Polarization via the Berry Phase Formalism" and Eq. (27)); higher η_{lp} in $CsGeCl_3$ indicates stronger lone-pair localization and polarization, while $CsGeI_3$ shows reduced values due to increased dielectric screening. This combined DFT–GW–BSE–ELF framework captures the interplay of lone-pair activity, A-site pressure, and screening in driving ferroelectricity in Rb-doped $CsGeX_3$.

Robustness and validation of the lone-pair localization index

Threshold dependence

The identification of lone-pair-rich regions in ELF maps requires selecting a color (or equivalently ELF-value) threshold. To assess the robustness of the localization index η_{lp} with respect to this choice, we repeated the full analysis over a broad range of hue thresholds corresponding to ELF values between approximately 0.50 and 0.75. Within this range, which spans the visually identifiable lone-pair lobes in all compounds, the absolute values of η_{lp} vary by less than 5%, while the relative trend $\eta_{\mathrm{lp}}(\mathrm{Cl}) > \eta_{\mathrm{lp}}(\mathrm{Br}) > \eta_{\mathrm{lp}}(\mathrm{I})$ is preserved in all cases. This stability reflects the fact that the Ge-centered lone-pair basins occupy a well-defined, contiguous region in ELF space rather than being confined to a narrow isovalue.

Slicing-plane dependence

ELF maps were primarily analyzed on the $[1\bar{1}0]$ crystallographic plane, which intersects the Ge–X framework and clearly resolves the asymmetric lobes associated with the stereochemically active Ge $4s^2$ lone pair. To assess the robustness of the lone-pair localization index with respect to plane selection, additional analyses were performed on symmetry-related and orthogonal planes, including $[10\bar{1}]$, $[110]$ and $[1\bar{1}0]$.

As expected, the absolute color intensity and local visual contrast of the ELF distribution around the Ge atom vary with slicing orientation, reflecting the anisotropic three-dimensional shape of the lone-pair electron density. Different planes emphasize different lobes of the nonbonding charge distribution. However, across all examined planes, the underlying chemical trend in electron localization remains invariant. In particular, the degree of localization consistently follows the sequence $CsGeCl_3$ > $CsGeBr_3$ > $CsGeI_3$, manifested both in higher ELF values and in more pronounced localized features around the Ge site in the chloride compared to the bromide and iodide compounds (see Figs. 7 and 5).

Quantitatively, while the detailed shape of the ELF contours depends on slicing orientation, the integrated lone-pair area A_{lp}, normalized by the total ELF-active area A_{ELF}, remains consistent within numerical uncertainty for all planes considered. This confirms that the lone-pair localization index η_{lp} captures an intrinsic three-dimensional localization property projected onto two-dimensional slices, rather than a plane-specific visualization artifact.

Overall, plane selection primarily affects the visual appearance of ELF maps but does not alter either the magnitude or the systematic trend of η_{lp}. The observed Cl $\to$ Br $\to$ I evolution therefore reflects a genuine chemical effect associated with changes in Ge–X bonding and lone-pair stereochemical activity, validating the use of η_{lp} as a robust and transferable descriptor of electronic localization in $CsGeX_3$ perovskites.

Segmentation and image-processing robustness

The Python-based image-processing pipeline employs color-space thresholding followed by morphological opening to isolate physically meaningful ELF regions while suppressing pixel-level noise. To evaluate sensitivity to segmentation parameters, we varied kernel sizes, mask smoothing operations, and image partitioning

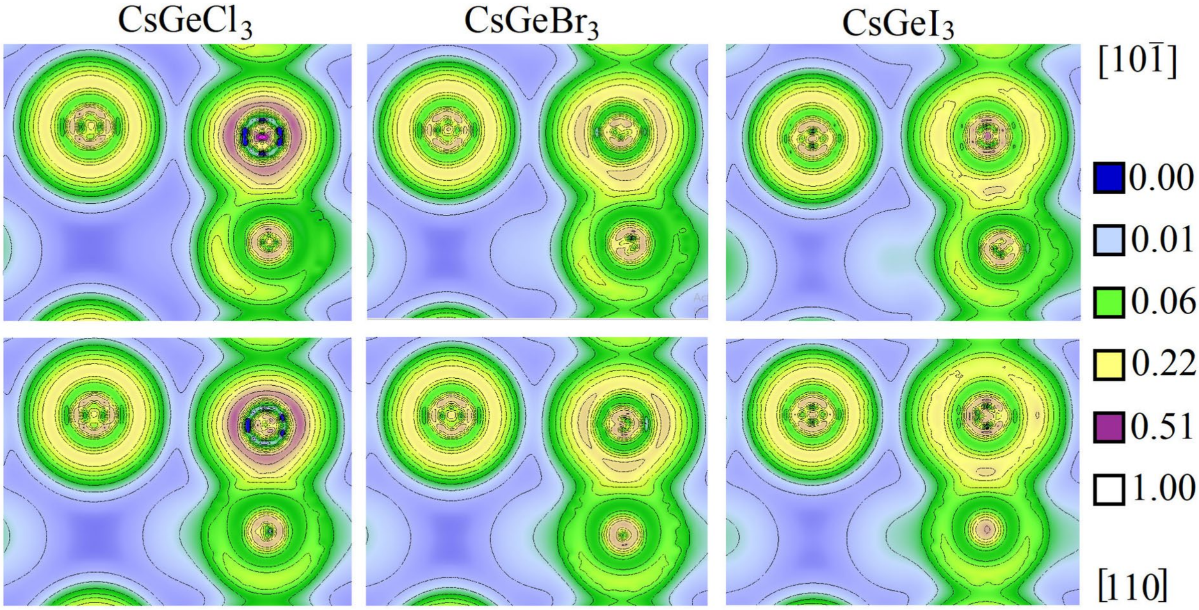

Fig. 7. ELF contour maps. Two-dimensional ELF contour maps for $CsGeCl_3$, $CsGeBr_3$, and $CsGeI_3$, shown on the $[10\bar{1}]$ (top row) and [110] (bottom row) crystallographic planes. This figure illustrates the stereochemically active lone-pair localization around the Ge atom. In each panel, the Cs atom is at the top-left, the halogen atom at the top-right, and the Ge atom at the bottom-right. Color scales represent ELF values from 0 (delocalized) to 1 (fully localized), with purple/yellow regions indicating enhanced localization associated with stereochemically active Ge $4s^2$ lone pairs. While the detailed shape and visual contrast of ELF contours vary with slicing orientation, the relative degree of localization follows a consistent chemical trend across all planes, with $CsGeCl_3$ exhibiting the strongest lone-pair localization, followed by $CsGeBr_3$ and $CsGeI_3$. This invariance confirms that the observed localization trends and the derived lone-pair localization index η_{lp} reflect intrinsic three-dimensional electronic structure rather than plane-dependent visualization artifacts.

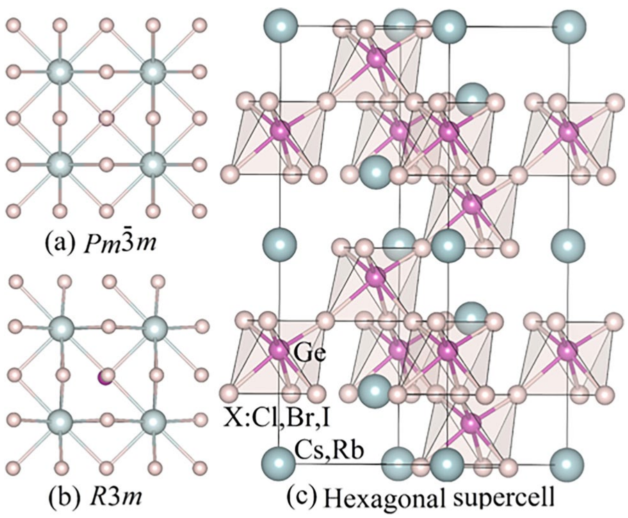

Fig. 8. Crystallographic structures of $CsGeX_3$ (X = Cl, Br, I). (**a**) Centrosymmetric cubic phase ($Pm\bar{3}m$) with inversion symmetry, (**b**) polar rhombohedral phase (*R*3*m*) exhibiting off-center Ge displacements and broken inversion symmetry along the body diagonal of the pseudo-cubic lattice (polar axis), and (**c**) $1 \times 1 \times 2$ hexagonal supercell with 16.67% Rb substitution on Cs sites. Ge atoms (purple) form corner-sharing GeX_6 octahedra with halogens (light pink), while Cs/Rb atoms (blue) occupy A-sites. The structural evolution from (**a**) to (**c**) visualizes symmetry lowering, octahedral tilting, and polar distortions that underlie ferroelectricity in $CsGeX_3$ perovskites. Panels (**a**) and (**b**) are projected onto the crystallographic YZ (*bc*) plane, perpendicular to the pseudo-cubic *a*-axis.

boundaries. These variations lead to negligible changes in η_{lp}, demonstrating that the extracted localization index is dominated by the macroscopic topology of the ELF distribution rather than by fine pixel-scale details. Importantly, the automated segmentation avoids subjective manual selection and ensures reproducibility across compositions and datasets.

Physical validation
The robustness of η_{lp} is further supported by its systematic correlation with independent physical observables. Across the $\mathrm{CsGeX_3}$ series, decreasing η_{lp} coincides with reduced spontaneous polarization P_s, increased dielectric screening, and weaker exciton binding energies. These correlations persist regardless of threshold or segmentation choice, confirming that η_{lp} reflects an intrinsic electronic-structure property associated with Ge $4s^2$ stereochemical activity rather than a visualization-dependent metric.

Doping-driven structural distortions in Rb-substituted $CsGeX_3$ halide perovskites
To model Rb substitution in $\mathrm{CsGeX_3}$ (X = Cl, Br, I), we use a $1 \times 1 \times 2$ supercell in the hexagonal setting of the rhombohedral *R*3*m* phase. Figure 8a, b compare the centrosymmetric $Pm\bar{3}m$ and polar *R*3*m* structures, where inversion symmetry is broken by asymmetric Ge off-centering and cooperative $\mathrm{GeX_6}$ tilts along $[001]_{\mathrm{hex}}$. These distortions generate net polarization via a second-order Jahn–Teller mechanism of the stereochemically active $\mathrm{Ge^{2+}}$ s^2 lone pair. In the low-symmetry phase, displacement of Ge along the pseudo-cubic body diagonal produces three longer Ge–Br bonds (3.146 Å) and three shorter ones (2.597 Å); along the Cs–Ge axis it yields one elongated bond (5.269 Å) and one contracted bond (4.837 Å), evidencing local symmetry breaking and anisotropic bonding, consistent with Ref.[1] (3.051/2.541 Å for long/short Ge–Br). The Rb-doped configuration in Fig. 8c applies chemical pressure via 16.7% A-site substitution ($\mathrm{Rb^+}$ 1.52 Å; $\mathrm{Cs^+}$ 1.67 Å), lowering the tolerance factor $t = \frac{r_{\mathrm{A}}+r_{\mathrm{X}}}{\sqrt{2}(r_{\mathrm{B}}+r_{\mathrm{X}})}$ and further amplifying these distortions. This supercell thus furnishes a symmetry-lowered, chemically consistent platform for high-fidelity first-principles simulations of ferroelectric, dielectric, and optical responses in lead-free halide perovskites.

Data availability
Data supporting the findings of this study are provided within the main paper, the Supplemental Material (SM). For transparency, the complete dataset and accompanying README file have also been uploaded to a private Figshare repository (https://doi.org/10.6084/m9.figshare.31332997). These materials contain the complete num erical results, input parameters, and documentation required for independent verification and reproducibility. Additional information can be made available upon rea- sonable request by contacting the corresponding author, Prof. Saeid Jalali-Asadabadi, at sjalali@sci.ui.ac.ir or saeid.jalali.asadabadi@gmail.com.

Received: 12 December 2025; Accepted: 19 February 2026
Published online: 28 February 2026

References
1. Zhang, Y. et al. Ferroelectricity in a semiconducting all-inorganic halide perovskite. *Sci. Adv.* **8**, eabj5881. https://doi.org/10.1126/sciadv.abj5881 (2022).
2. Wang, J. et al. Highly efficient all-inorganic perovskite solar cells with suppressed non-radiative recombination by a Lewis base. *Nat. Commun.* **11**, 177. https://doi.org/10.1038/s41467-019-13909-5 (2020).
3. Thi Han, N., Khuong Dien, V. & Lin, M.-F. Electronic and optical properties of $\mathrm{CsGeX_3}$ (X= Cl, Br, and I) compounds. *ACS Omega* **7**, 25210–25218. https://doi.org/10.1021/acsomega.2c02088 (2022).
4. Jung, H. S. & Park, N.-G. Perovskite solar cells: From materials to devices. *Small* **11**, 10–25. https://doi.org/10.1002/smll.201402767.
5. Correa-Baena, J.-P. et al. Promises and challenges of perovskite solar cells. *Science* **358**, 739–744. https://doi.org/10.1126/science.aam6323 (2017).
6. Pal, S., Swain, A. B., Biswas, P. P. & Murugavel, P. Photoferroelectric phenomena in ferroelectric oxides and a Rayleigh analysis. *Phys. Rev. Mater.* **4**, 064415. https://doi.org/10.1103/PhysRevMaterials.4.064415 (2020).
7. Li, Y. & Li, Y. All-Inorganic Perovskite Solar Cells. Chap. 5. 175–221 (Wiley, 2021).
8. Zhang, J., Hodes, G., Jin, Z. & Liu, S. F. All-inorganic $\mathrm{CsPbX_3}$ perovskite solar cells: Progress and prospects. *Angew. Chem. Int. Ed.* **58**, 15596–15618. https://doi.org/10.1002/anie.201901081 (2019).
9. Jiang, Y. et al. Reduced-dimensional α-$\mathrm{CsPbX_3}$ perovskites for efficient and stable photovoltaics. *Joule* **2**, 1356–1368. https://doi.org/10.1016/j.joule.2018.05.004 (2018).
10. Mali, S. S. et al. Phase-heterojunction all-inorganic perovskite solar cells surpassing 21.5% efficiency. *Nat. Energy* **8**, 989–1001. 10.1038/s41560-023-01310-y (2023).
11. Chu, X. et al. Surface in situ reconstruction of inorganic perovskite films enabling long carrier lifetimes and solar cells with 21% efficiency. *Nat. Energy* **8**, 372–380. 10.1038/s41560-023-01220-z (2023).
12. Zhang, H. et al. Lead immobilization for environmentally sustainable perovskite solar cells. *Nature* **617**, 687–695. https://doi.org/10.1038/s41586-023-05938-4 (2023).
13. Huang, L.-Y. & Lambrecht, W. R. L. Vibrational spectra and nonlinear optical coefficients of rhombohedral $\mathrm{CsGe}\ X_3$ halide compounds with $x = \mathrm{I}$, Br, Cl. *Phys. Rev. B* **94**, 115202 (2016).
14. Dias, A. C., Lima, M. P. & Da Silva, J. L. F. Role of structural phases and octahedra distortions in the optoelectronic and excitonic properties of $\mathrm{CsGeX_3}$ (X = Cl, Br, I) perovskites. *J. Phys. Chem. C* **125**, 19142–19155. https://doi.org/10.1021/acs.jpcc.1c05245 (2021).
15. Saliba, M. et al. Cesium-containing triple cation perovskite solar cells: Improved stability, reproducibility and high efficiency. *Energy Environ. Sci.* **9**, 1989–1997. https://doi.org/10.1039/C5EE03874J (2016).
16. Rahaman, M. Z. & Hossain, A. K. M. A. Effect of metal doping on the visible light absorption, electronic structure and mechanical properties of non-toxic metal halide $\mathrm{CsGeCl_3}$. *RSC Adv.* **8**, 33010–33018. https://doi.org/10.1039/C8RA06374E (2018).
17. Chen, R. et al. Polarization controlled photocurrent in perovskite $\mathrm{CsGeX_3}$ (X = Cl, Br, I). *J. Phys. Chem. C* **127**, 19788–19795. https://doi.org/10.1021/acs.jpcc.3c04619 (2023).
18. Scott, J. F. Applications of modern ferroelectrics. *Science* **315**, 954–959. https://doi.org/10.1126/science.1129564 (2007).

19. Martin, L. W. & Rappe, A. M. Thin-film ferroelectric materials and their applications. *Nat. Rev. Mater.* **2**, 1–14. https://doi.org/10.1038/natrevmats.2016.87 (2016).
20. Rezaei nik, Y., Reyhani, A., Farjami-Shayesteh, S. & Mortazavi, S. Photocurrent enhancement of hybrid perovskite $CsGeBr_3$ assisted two-dimensional WS_2 nano-flakes based on electron-hole mobility improvement. *Opt. Mater*. **112**, 110754. 10.1016/j.optmat.2020.110754 (2021).
21. Li, T. et al. Optical control of polarization in ferroelectric heterostructures. *Nat. Commun.* **9**, 1–8. https://doi.org/10.1038/s41467-018-05640-4 (2018).
22. Huang, H. Ferroelectric photovoltaics. *Nat. Photon.* **4**, 134–135. https://doi.org/10.1038/nphoton.2010.15 (2010).
23. Wei, L. et al. Giant optical absorption and ferroelectric polarization of $BiCoO_2S$ perovskite oxysulfide by first principles prediction. *Phys. Chem. Chem. Phys.* **22**, 11382–11391. https://doi.org/10.1039/D0CP00057D (2020).
24. Ming, W., Shi, H. & Du, M.-H. Large dielectric constant, high acceptor density, and deep electron traps in perovskite solar cell material $CsGeI_3$. *J. Mater. Chem. A* **4**, 13852–13858. https://doi.org/10.1039/C6TA04685A (2016).
25. Yadav, K. & Ray, N. Assessing the impact of triaxial strain on carrier mobility and dielectric properties in cubic $CsBCl_3$ (B = Pb, Sn, or Ge) perovskites: A first principles study. *AIP Adv.* **13**, 125304. https://doi.org/10.1063/5.0181531 (2023).
26. Zhong, C.-J. et al. Theoretical study on photoelectric properties of ferroelectric photovoltaic perovskite $CsGeBr_3$ based on first-principle calculations. *Physica Scripta* **99**, 065982. https://doi.org/10.1088/1402-4896/ad4749 (2024).
27. Islam, M. A., Islam, J., Islam, M. N., Sen, S. K. & Hossain, A. K. M. A. Enhanced ductility and optoelectronic properties of environment-friendly $CsGeCl_3$ under pressure. *AIP Adv.* **11**, 045014. https://doi.org/10.1063/5.0048849 (2021).
28. Schwarz, U., Wagner, F., Syassen, K. & Hillebrecht, H. Effect of pressure on the optical-absorption edges of csgebr_3 and csgecl_3. *Phys. Rev. B* **53**, 12545–12548. https://doi.org/10.1103/PhysRevB.53.12545 (1996).
29. H.-E., M. M. S., Alsobhi, B. & Almeshal, A. Tuning of band gap and enhancing electronic properties of $CsSnBr_3$ under high pressure for optoelectronic applications. *Comput. Condens. Matter* **38**, e00870. 10.1016/j.cocom.2023.e00870 (2024).
30. Radha, S. K., Bhandari, C. & Lambrecht, W. R. L. Distortion modes in halide perovskites: To twist or to stretch, a matter of tolerance and lone pairs. *Phys. Rev. Mater.* **2**, 063605. https://doi.org/10.1103/PhysRevMaterials.2.063605 (2018).
31. Jong, U.-G. et al. First-principles study on structural, electronic, and optical properties of inorganic Ge-based halide perovskites. *Inorg. Chem.* **58**, 4134–4140. https://doi.org/10.1021/acs.inorgchem.8b03095 (2019).
32. Men, L., Rosales, B. A., Gentry, N. E., Cady, S. D. & Vela, J. Lead-free semiconductors: Soft chemistry, dimensionality control, and manganese-doping of germanium halide perovskites. *ChemNanoMat* **5**, 334–339. https://doi.org/10.1002/cnma.201800497 (2019).
33. Zhang, X. et al. Strong blue emission from Sb^{3+}-doped super small $CsPbBr_3$ nanocrystals. *J. Phys. Chem. Lett.* **10**, 1750–1756. 10.1021/acs.jpclett.9b00790 (2019).
34. Bala, A. & Kumar, V. Stability of the Eu^{2+} dopant in $CsPbBr_3$ perovskites: A first-principles study. *J. Phys. Chem. C* **123**, 6965–6969. https://doi.org/10.1021/acs.jpcc.8b10261 (2019).
35. Hohenberg, P. & Kohn, W. Inhomogeneous electron gas. *Phys. Rev.* **136**, B864–B871. https://doi.org/10.1103/PhysRev.136.B864 (1964).
36. Kohn, W. & Sham, L. J. Self-consistent equations including exchange and correlation effects. *Phys. Rev.* **140**, A1133–A1138. https://doi.org/10.1103/PhysRev.140.A1133 (1965).
37. Sharifzadeh, S. Many-body perturbation theory for understanding optical excitations in organic molecules and solids. *J. Phys. Condens. Matter* **30**, 153002. 10.1088/1361-648X/aab0d1 (2018).
38. Azadparvar, M., Rahnamaye Aliabad, H. A. & Özdemir, E. G. Optoelectronic and thermoelectric properties of Sb_2S_3 under hydrostatic pressure for energy conversion. *AIP Adv.* **13**, 065218. https://doi.org/10.1063/5.0151650 (2023).
39. Azeem, W. et al. Investigation of semiconductor to metallic transitions of perovskite $CsGeCl_3$ material through induced pressure: A DFT calculation for photovoltaic and optoelectronic applications. *Mater. Renew. Sustain. Energy* **14**, 1 (2025).
40. Qu, J. et al. Origin of pressure-induced nonlinear optical property enhancement in $CsGeCl_3$ perovskite: $[GeCl_6]$ octahedron distortion and band gap closing. *J. Am. Chem. Soc.* **147**, 6717–6726. https://doi.org/10.1021/jacs.4c16182 (2025).
41. Seo, D.-K., Gupta, N., Whangbo, M.-H., Hillebrecht, H. & Thiele, G. Pressure-induced changes in the structure and band gap of $CsGeX_3$ (X = Cl, Br) studied by electronic band structure calculations. *Inorg. Chem.* **37**, 407–410. https://doi.org/10.1021/ic970659e (1998).
42. Enhanced dielectric, magnetic and optical properties of Cr-doped $BiFeO_3$ multiferroic nanoparticles synthesized by sol-gel route. *Results Phys*. **13**, 102299. 10.1016/j.rinp.2019.102299 (2019).
43. Even, J., Pedesseau, L., Jancu, J.-M. & Katan, C. Dft and $k \cdot p$ modelling of the phase transitions of lead and tin halide perovskites for photovoltaic cells. *Phys. Status Solidi RRL* **8**, 31–35. https://doi.org/10.1002/pssr.201308183 (2014).
44. Castelli, I. E., García-Lastra, J. M., Thygesen, K. S. & Jacobsen, K. W. Bandgap calculations and trends of organometal halide perovskites. *APL Mater.* **2**, 081514. https://doi.org/10.1063/1.4893495 (2014).
45. Lin, Z.-G., Tang, L.-C. & Chou, C.-P. Study on mid-IR NLO crystals $\mathrm{CsGe(Br_xCl_{1-x})_3}$. *Opt. Mater.* **31**, 28–34. https://doi.org/10.1016/j.optmat.2008.01.004 (2008).
46. Xiang, G. et al. Strain-induced bandgap engineering in $CsGeX_3$ (X = I, Br or Cl) perovskites: Insights from first-principles calculations. *Phys. Chem. Chem. Phys.* **24**, 5448–5454. https://doi.org/10.1039/D1CP05787A (2022).
47. Saliba, M. et al. Incorporation of rubidium cations into perovskite solar cells improves photovoltaic performance. *Science* **354**, 206–209. https://doi.org/10.1126/science.aah5557 (2016).
48. Syzgantseva, O. A., Saliba, M., Grätzel, M. & Rothlisberger, U. Stabilization of the perovskite phase of formamidinium lead triiodide by methylammonium, Cs, and/or Rb doping. *J. Phys. Chem. Lett.* **8**, 1191–1196. https://doi.org/10.1021/acs.jpclett.6b03014 (2017).
49. Jacobsson, T. J. et al. Extending the compositional space of mixed lead halide perovskites by Cs, Rb, K, and Na doping. *J. Phys. Chem. C* **122**, 13548–13557. https://doi.org/10.1021/acs.jpcc.7b12464 (2018).
50. Chelil, N., Sahnoun, M., Benhalima, Z., Larbi, R. & Eldin, S. M. Insights into the relationship between ferroelectric and photovoltaic properties in $CsGeI_3$ for solar energy conversion. *RSC Adv.* **13**, 1955–1963. https://doi.org/10.1039/D2RA06860E (2023).
51. Dawber, M., Rabe, K. M. & Scott, J. F. Physics of thin-film ferroelectric oxides. *Rev. Mod. Phys.* **77**, 1083–1130. https://doi.org/10.1103/RevModPhys.77.1083 (2005).
52. Shigenari, T. Raman spectra of soft modes in ferroelectric crystals. In *Ferroelectric Materials-Synthesis and Characterization* (IntechOpen, 2015).
53. Jamal, M., Bilal, M., Ahmad, I. & Jalali-Asadabadi, S. Irelast package. *J. Alloys Compd.* **735**, 569–579. https://doi.org/10.1016/j.jallcom.2017.10.139 (2018).
54. Hybertsen, M. S. & Louie, S. G. Electron correlation in semiconductors and insulators: Band gaps and quasiparticle energies. *Phys. Rev. B* **34**, 5390–5413. https://doi.org/10.1103/PhysRevB.34.5390 (1986).
55. Hedin, L. New method for calculating the one-particle Green's function with application to the electron-gas problem. *Phys. Rev.* **139**, A796–A823. https://doi.org/10.1103/PhysRev.139.A796 (1965).
56. Salpeter, E. E. & Bethe, H. A. A relativistic equation for bound-state problems. *Phys. Rev.* **84**, 1232–1242. https://doi.org/10.1103/PhysRev.84.1232 (1951).
57. Onida, G., Reining, L. & Rubio, A. Electronic excitations: Density-functional versus many-body Green's-function approaches. *Rev. Mod. Phys.* **74**, 601–659. https://doi.org/10.1103/RevModPhys.74.601 (2002).
58. Leng, X., Jin, F., Wei, M. & Ma, Y. GW method and Bethe-Salpeter equation for calculating electronic excitations. *WIREs Comput. Mol. Sci.* **6**, 532–550. https://doi.org/10.1002/wcms.1265 (2016).

59. Blase, X., Duchemin, I., Jacquemin, D. & Loos, P.-F. The Bethe-Salpeter equation formalism: From physics to chemistry. *J. Phys. Chem. Lett*. **11**, 7371–7382. 10.1021/acs.jpclett.0c01875 (2020).
60. Strinati, G. Application of the Green's functions method to the study of the optical properties of semiconductors. *La Rivista del Nuovo Cimento* **1978–1999**(11), 1–86. https://doi.org/10.1007/BF02725962 (1988).
61. Sagmeister, S. & Ambrosch-Draxl, C. Time-dependent density functional theory versus Bethe-Salpeter equation: An all-electron study. *Phys. Chem. Chem. Phys.* **11**, 4451–4457. https://doi.org/10.1039/B903676H (2009).
62. Gillet, Y. Ab initio study of Raman and optical spectra of crystalline materials and their temperature dependence. PhD Thesis, Université Catholique de Louvain, Louvain-la-Neuve (2017).
63. Rahimi, S., Ebrahimi-Jaberi, R., Jalali-Asadabadi, F., Mollabashi, L. & Jalali-Asadabadi, S. Influence of (Ba, F) multidoping on structural, magnetic, optical, and electrical properties as well as performance enhancement of multiferroic $\mathrm{BiFeO_3}$. *Phys. Rev. B* **106**, 115205. https://doi.org/10.1103/PhysRevB.106.115205 (2022).
64. Sander, T., Maggio, E. & Kresse, G. Beyond the Tamm-Dancoff approximation for extended systems using exact diagonalization. *Phys. Rev. B* **92**, 045209. https://doi.org/10.1103/PhysRevB.92.045209 (2015).
65. Doumont, J., Tran, F. & Blaha, P. Implementation of self-consistent MGGA functionals in augmented plane wave based methods. *Phys. Rev. B* **105**, 195138. https://doi.org/10.1103/PhysRevB.105.195138 (2022).
66. Neupane, B., Tang, H., Nepal, N. K., Adhikari, S. & Ruzsinszky, A. Opening band gaps of low-dimensional materials at the meta-GGA level of density functional approximations. *Phys. Rev. Mater.* **5**, 063803. https://doi.org/10.1103/PhysRevMaterials.5.063803 (2021).
67. Berry, M. Classical adiabatic angles and quantal adiabatic phase. *J. Phys. A: Math. Gen.* **18**, 15. https://doi.org/10.1088/0305-4470/18/1/012 (1985).
68. Ahmed, S. et al. BerryPI: A software for studying polarization of crystalline solids with $\mathrm{WIEN\ 2\ k}$ density functional all-electron package. *Comput. Phys. Commun.* **184**, 647–651. https://doi.org/10.1016/j.cpc.2012.10.028 (2013).
69. Vanderbilt, D. Berry-phase theory of proper piezoelectric response. *J. Phys. Chem. Solids* **61**, 147–151. https://doi.org/10.1016/S0022-3697(99)00273-5 (2000).
70. Berry, M. V. Quantal phase factors accompanying adiabatic changes. *Proc. R. Soc. A* **392**, 45–57. https://doi.org/10.1098/rspa.1984.0023 (1984).
71. Xiao, D., Chang, M.-C. & Niu, Q. Berry phase effects on electronic properties. *Rev. Mod. Phys.* **82**, 1959–2007. https://doi.org/10.1103/RevModPhys.82.1959 (2010).
72. Rahimi, S., Jalali-Asadabadi, S., Blaha, P. & Jalali-Asadabadi, F. Nonzero spontaneous electric polarization in metals: novel predictive methods and applications. *Sci. Rep.* **14**, 672. https://doi.org/10.1038/s41598-023-49463-w (2024).
73. Bader, R. F. W. A quantum theory of molecular structure and its applications. *Chem. Rev.* **91**, 893–928 (1991).
74. Bader, R. F. W. *Atoms in Molecules: A Quantum Theory (International Series of Monographs on Chemistry)* (Oxford University Press, 1994).
75. de-la Roza, A. O., Blanco, M., Pendás, A. M. & Luaña, V. Critic: A new program for the topological analysis of solid-state electron densities. *Comput. Phys. Commun*. **180**, 157–166 (2009).
76. de-la Roza, A. O., Johnson, E. R. & Luaña, V. Critic2: A program for real-space analysis of quantum chemical interactions in solids. *Comput. Phys. Commun*. **185**, 1007–1018 (2014).
77. Yazdani-Kachoei, M., Jalali-Asadabadi, S. & Arianmehr, N. Topological analysis of $\mathrm{CeMIn_5}$ (M = Co, Rh) electron charge densities. *Comput. Mater. Sci.* **164**, 205–217. https://doi.org/10.1016/j.commatsci.2019.03.041 (2019).
78. Yazdani-Kachoei, M. & Jalali-Asadabadi, S. Topological analysis of electron density in half-Heusler ZrXBi (X = Co, Rh) compounds: A density functional theory study accompanied by Bader's quantum theory of atoms in molecules. *J. Alloys Compd.* **828**, 154287. https://doi.org/10.1016/j.jallcom.2020.154287 (2020).
79. Koumpouras, K. & Larsson, J. A. Distinguishing between chemical bonding and physical binding using electron localization function (ELF). *J. Phys. Condens. Matter* **32**, 315502. 10.1088/1361-648X/ab7fd8 (2020).
80. Gulans, A. et al. exciting: a full-potential all-electron package implementing density-functional theory and many-body perturbation theory. *J. Phys. Condens. Matter* **26**, 363202. 10.1088/0953-8984/26/36/363202 (2014).
81. Sjöstedt, E., Nordström, L. & Singh, D. An alternative way of linearizing the augmented plane-wave method. *Solid State Commun.* **114**, 15–20. https://doi.org/10.1016/S0038-1098(99)00577-3 (2000).
82. Perdew, J. P., Burke, K. & Ernzerhof, M. Generalized gradient approximation made simple. *Phys. Rev. Lett.* **77**, 3865 (1996).
83. Callaway, J. *Quantum Theory of the Solid State* (Academic Press, 2013).
84. Yalameha, S., Nourbakhsh, Z. & Vashaee, D. Elatools: A tool for analyzing anisotropic elastic properties of the 2D and 3D materials. *Comput. Phys. Commun.* **271**, 108195. https://doi.org/10.1016/j.cpc.2021.108195 (2022).
85. Ravindran, P. et al. Density functional theory for calculation of elastic properties of orthorhombic crystals: $\mathrm{Application\ to\ TiSi_2}$. *J. Appl. Phys.* **84**, 4891–4904. https://doi.org/10.1063/1.368733 (1998).
86. Schiltz, R. J. & Smith, J. F. Elastic constants of some $\mathrm{MAl_2}$ single crystals. *J. Appl. Phys.* **45**, 4681–4685. https://doi.org/10.1063/1.1663118 (1974).
87. Sanati, M., Albers, R. C., Lookman, T. & Saxena, A. Elastic constants, phonon density of states, and thermal properties of $\mathrm{UO_2}$. *Phys. Rev. B* **84**, 014116. https://doi.org/10.1103/PhysRevB.84.014116 (2011).
88. Shafiq, M. et al. Elastic and mechanical properties of lanthanide monoxides. *J. Alloys Compd.* **618**, 292–298. https://doi.org/10.1016/j.jallcom.2014.08.171 (2015).
89. Zeng, X. et al. Pressure effect on elastic constants and related properties of $\mathrm{Ti_3\ Al}$ intermetallic compound: A first-principles study. *Materials* **11**. https://doi.org/10.3390/ma11102015
90. Shang, S. L. et al. Structural, vibrational, and thermodynamic properties of ordered and disordered $\mathrm{Ni_{1-x}\ Pt_x}$ alloys from first-principles calculations. *Phys. Rev. B* **83**, 144204. https://doi.org/10.1103/PhysRevB.83.144204 (2011).
91. Blaha, P. et al. *WIEN2k. An Augmented Plane Wave + Local Orbitals Program for Calculating Crystal Properties*. (2021).
92. Jamal, M., Jalali Asadabadi, S., Ahmad, I. & Rahnamaye Aliabad, H. Elastic constants of cubic crystals. *Comput. Mater. Sci.* **95**, 592–599. 10.1016/j.commatsci.2014.08.027 (2014).
93. Ebrahimi-Jaberi, R. & Jalali-Asadabadi, S. Elasticity and stability of gdal2 under pressure and temperature investigated using dft+ai. *Sci. Rep.* **15**, 15573. https://doi.org/10.1038/s41598-025-99186-3 (2025).
94. Iqbal, R., Bilal, M., Jalali-Asadabadi, S., Rahnamaye Aliabad, H. A. & Ahmad, I. Theoretical investigation of thermoelectric and elastic properties of intermetallic compounds $\mathrm{ScTM\ (TM = Cu,\ Ag,\ Au\ and\ Pd)}$. *Int. J. Mod. Phys. B* **32**, 1850004. https://doi.org/10.1142/S0217979218500042 (2018).
95. Ebrahimi-Jaberi, R. & Jalali-Asadabadi, S. Anisotropic mechanical behavior and thermal attributes of antiferromagnetic $\mathrm{UX_2(\ X\ =\ P}$, As, Sb) materials: Adensity functional and elasticity theories study. *Mater. Chem. Phys.* **312**, 128590. https://doi.org/10.1016/j.matchemphys.2023.128590.

Acknowledgements

This work forms part of the postdoctoral research project of Shahrbano Rahimi, supervised by Prof. Saeid Jalali-Asadabadi, and supported by the Iran National Science Foundation (INSF) under Grant No. 4027749, dated 1403/03/08. The authors gratefully acknowledge the University of Isfahan for its non-financial support and for hosting the research activities associated with this project.

Author contributions

S.R.: Conceptualization, Data Curation, Formal Analysis, Investigation, Methodology, Validation, Visualization, Writing - Initial Draft. S.J.-A.: Conceptualization, Data Curation, Formal Analysis, Funding Acquisition, Investigation, Methodology, Project Administration, Resources, Software, Supervision, Validation, Visualization, Writing - Original Manuscript, Writing - Review & Editing, Finalization, Corresponding Author.

Funding

This research received no project-specific funding. The Iran National Science Foundation (INSF) fellowship (Grant No. 4027749) covers only the postdoctoral position and does not include research funds. The University of Isfahan (UI) provided institutional hosting without financial support.

Declarations

Competing interests

The authors declare no competing interests.

Additional information

Supplementary Information The online version contains supplementary material available at https://doi.org/10.1038/s41598-026-41305-9.

Correspondence and requests for materials should be addressed to S.J.-A.

Reprints and permissions information is available at www.nature.com/reprints.

Publisher's note Springer Nature remains neutral with regard to jurisdictional claims in published maps and institutional affiliations.